High-Resolution UV Absorption Cross-section Measurements of ^{32}S, ^{33}S, ^{34}S, and ^{36}S Sulfur Dioxide for the $\tilde{B}^1B_1$-$\tilde{X}^1A_1$ Absorption Band

Y. Li[1], S. O. Danielache[1], Y. Endo[2], S. Nanbu[1], Y. Ueno[2,3,4]

[1]Department of Materials and Life Science, Faculty of Science and Technology, Sophia University, Japan
[2]Department of Earth and Planetary Sciences, Tokyo Institute of Technology, Tokyo, Japan
[3]Earth-Life Science Institute, Tokyo Institute of Technology, Tokyo, Japan
[4]Institute for Extra-cutting-edge Science and Technology Avant-garde Research (X-star), Super-cutting-edge Grand and Advanced Research (SUGAR) Program, Japan Agency for Marine-Earth Science and Technology (JAMSTEC), Yokosuka, Japan
Corresponding author: Yuanzhe Li (liyuanzhe@eagle.sophia.ac.jp)

Key Points:

- We report measured cross-sections of $^{32}SO_2$, $^{33}SO_2$, $^{34}SO_2$, $^{36}SO_2$ for the $\tilde{B}^1B_1$-$\tilde{X}^1A_1$ absorption band over the wavelength range 240 to 320 nm at a resolution of 0.4 cm^{-1}.
- A least absolute deviation linear regression method was applied to calculate the cross-sections, and the error bars on the measured cross-sections ranged between 3 and 10%.
- Reported absorption cross-sections predict relatively small mass-independent fractionation (^{33}E = −0.8±0.2‰ and ^{36}E = −4.0±0.4‰) during SO_2 photoexcitation for top of the atmosphere solar spectra.

Abstract

High-resolution and high-precision spectrum data presents a challenging measurement. We report newly measured ultraviolet absorption cross-sections of $^{32}SO_2$, $^{33}SO_2$, $^{34}SO_2$, and $^{36}SO_2$ for the $\tilde{B}^1B_1$-$\tilde{X}^1A_1$ band over the wavelength range 240 to 320 nm at a resolution of 0.4 cm^{-1}. The resolution is improved by 20 times compared to a previous study (Danielache et al., 2012). A least absolute deviation linear regression method was applied to calculate the cross-sections and spectral errors from a set of measurements recorded at a wide range of pressure to ensure optimal signal-to-noise ratio at all wavelengths. Based on this analysis, error bars on the measured cross-sections ranged between 3 and 10%. The overall features of measured cross-sections, such as peak positions of isotopologues, are consistent with previous studies. We provide improved spectral data for studying sulfur mass-independent fraction (S-MIF) signatures in SO_2 photoexcitation. Our spectral measurements predict that SO_2 photoexcitation produces $^{33}E = -0.8\pm0.2$‰ and $^{36}E = -4.0\pm0.4$‰, whose magnitudes are smaller than those reported by Danielache et al. (2012).

1 Introduction

Sulfur dioxide (SO_2) is the most common reduced sulfur compound present in many planetary atmospheres. This molecule has been known to exist in Earth, Venus, and Io for many years (Yung and DeMore, 1999). It has also been reported the presence of SO_2 in the atmosphere of WASP-39b (Tsai et al., 2023). Understanding the photochemical properties of this molecule is essential for geochemical studies of planetary atmospheres. Its interactions with UV light trigger a cascade of chemical reactions that produce a variety of compounds, such as sulfuric acid (H_2SO_4) or S_8, depending on the atmospheric redox state.

Stable isotopes are a powerful tool for studying and understanding a variety of geochemical processes. Such applications involve singly substituted isotopes, a combination of the same isotope with different masses which creates mass-dependent and mass-independent relations, and more than one isotope within the same molecule known as clumped isotopes (e.g., Eiler et al., 2014). The sulfur mass-independent fractionation (S-MIF) signatures (non-zero $\Delta^{33}S$ and $\Delta^{36}S$ values) in the geological record have been shown to be non-zero before ~2.3 Ga coinciding with the rise of oxygen levels in the atmosphere (Farquhar et al., 2000; Ono, 2017). Studies by Farquhar and co-workers (Farquhar et al., 2001; Masterson et al., 2011) and subsequent chemical chamber experiments (Endo et al., 2019; Endo et al., 2016) have shown that SO_2 photodissociation and photoexcitation reactions under conditions free of oxygen produce large S-MIF signatures, although the previous experiments have not fully reproduced the Archean record such as relationships between $\Delta^{33}S$ and $\Delta^{36}S$ and between $\delta^{34}S$ and $\Delta^{33}S$ (e.g., Ono, 2017; Endo et al., 2022b). An atmospheric photochemical model study by Pavlov and Kasting (2002) showed that SO radical produced during photolysis rapidly oxidized back to SO_2 with 10^{-5} of present atmospheric levels of O_2 and therefore setting a maximum level of atmospheric oxygen abundance in which the S-MIF can be preserved, yet no model study has succussed into reproducing the geological record. The work done to constrain the mechanisms and the atmospheric conditions that explain the S-MIF in the geological record is extensive and

a full summary is beyond the scope of this report (e.g., Ono, 2017; Thiemens and Lin, 2019) but current understanding points to a combination of mechanisms including the photoexcitation $\tilde{B}^1B_1$-$\tilde{X}^1A_1$band of the SO_2 molecule (Endo et al., 2016).

In the present earth, sulfur aerosols produced in the lower stratosphere from material uplifted by plumes during Plinian eruptions and collected from Antarctic and Greenland ice cores show an S-MIF signature distinct from Archean sulfides and sulfates (Baroni et al., 2007). Hattori et al. (2013), based on the data reported by Danielache et al. (2012), reported that SO_2 photoexcitation in the lower stratosphere produce signals compatible with the ice core record. A subsequent study presented by Whitehill et al. (2013) showed that the fate of the photoexcited fragment is not only direct oxidation by O_2, as assumed in the Hattori et al. (2013) study, but follows a branching mechanism due to quenching in which a fraction of the molecules in the $\tilde{A}^1A_2/\tilde{B}^1B_1$ state are converted to the $\tilde{a}^3B_1$ state. They further show an isotope selective spin-orbit interaction between the singlet ($\tilde{A}^1A_2/\tilde{B}^1B_1$) and triplet ($\tilde{a}^3B_1$) manifolds. Despite the extensive work done so far, further quantification of the isotopic effect during the $\tilde{B}^1B_1$-$\tilde{X}^1A_1$and $\tilde{A}^1A_2$-$\tilde{X}^1A_1$ excitation is needed.

The highly structured SO_2 UV absorption spectrum directly results from electronic transitions and a complex and nuanced set of vibrational and rotational energy levels (Herzberg, 1945). The single report on the $^{32}SO_2$, $^{33}SO_2$, $^{34}SO_2$, and $^{36}SO_2$ (hereafter $^{32,33,34,36}SO_2$) $\tilde{B}^1B_1$-$\tilde{X}^1A_1$ absorption spectrum from Danielache et al. (2012) has a spectral resolution of 8 cm^{-1} which is still far from fully resolved (Stark et al., 1999). Although from the $\tilde{C}^1B_2$-$\tilde{X}^1A_1$ absorption band, spectral measurements by Endo et al. (2015), SO_2 column density dependence on cross-sections were observed (especially, this apparent column density and cross-sections relation was stronger at absorption peaks; see Endo et al., 2015 Figure 1). Further analysis suggested that insufficient spectral resolution relative to absorption line width explains this phenomenon (Endo et al., 2015). The lack of resolution directly affects the peak separation and further interferes with the accuracy of S-MIF calculations, which would significantly impact the study of light-induced isotopic effects (See Endo et al., 2015 Figure S1). High-resolution spectrum is therefore necessary for better understanding spectroscopic properties and accurately the absorption spectra (Wu et al., 2000). Fully resolved spectra (Koplow et al., 1998) with a low level of noise would be the authoritative yet near unachievable measurement for an entire absorption band.

Recent studies by Lyons et al. (2018) have reported pressure room temperature broadening coefficients of 0.30 ± 0.03 cm^{-1} atm^{-1} and 0.40 ± 0.04 cm^{-1} atm^{-1} for N_2 and CO_2 respectively for the $\tilde{C}$ -$\tilde{X}$ absorption band and Leonard (1989) reported broadening coefficients of 0.237 ± 0.0011 cm^{-1} atm^{-1} and 0.325 ± 0.0015 cm^{-1} atm^{-1} for N_2 and CO_2 respectively for the $\tilde{B}$ -$\tilde{X}$ absorption band. There are studies suggesting a largely congested line profile for the SO_2 electronic spectra. The basis for such an assertion are from theoretical calculations of the bound-type exited electronic states coupled to rotational-vibrational transitions (Kumar et al., 2015). Models reported by Lyons et al. (2018) used a line spacing of 0.25 cm^{-1} for the $\tilde{C}$ -$\tilde{X}$ band which is not the absorption band concerned in this report, but it might show a similar behavior. A quantitative assessment of natural widths and line congestion at different spectral regions is yet to be reported. The computational requirement for a theoretical calculation of a high *J* electronic spectrum is a challenge to be reckoned with. Reports on *J* and *K* values (*J* and

105 *K* stand for rotational and vibrational wavefunction, not to be confused with the integrated
106 photo-dissociation rate constant *J*) such as the reported by Kumar et al. (2015) for total angular
107 momentum $J = 0–10$ are illustrative of the amount of computations needed for a full spectrum
108 calculated at high *J*. Pressure broadening coefficients put together with the above suggested
109 line density of these systems will cause line profile overlap and thus creating a pseudo-
110 broadened spectra or sections of the most congested parts of the rovibrational progression and
111 thus reducing the minimal requirement of spectral resolution for meaningful photo-induced
112 isotopic effects. In summary, a combination of spectral resolution, pressure broadening, and
113 profile overlap suggests that the data in this report might be suitable for the study of isotopic
114 effects happening in a planetary atmosphere with a total atmospheric pressure close to 1 atm.
115 An additional known issue is that even if a fully resolved spectrum is achieved, it is difficult
116 to obtain high precision with high-resolution measurements because the noise increases at high-
117 resolution measurements (see comparison in Table 1). The issue would lead to large errors of
118 calculated photodissociation rate constants and associated isotopic effects. In order to address
119 this issue we have implemented a linear regression method that has been widely used in Fourier
120 transform spectroscopy to reduce noise and increase spectral precision (Barra et al., 2021;
121 Dreissig et al., 2009; Meyer-Jacob et al., 2014; Santos et al., 2021).
122 In this study, an experimental setup of a Fourier transform spectrometer (VERTEX 80v, Bruker,
123 Japan) was optimized to adapt measurements in the UV band. We used the least absolute
124 deviation (LAD) linear regression for data calibration and measured the $^{32}SO_2$, $^{33}SO_2$, $^{34}SO_2$,
125 and $^{36}SO_2$, $\tilde{B}^1B_1$-$\tilde{X}^1A_1$ absorption spectrum ranges from 240 to 320 nm with a resolution of
126 0.4 cm^{-1} and 3−10% of error.

127 ## 2 Experimental

128 ### 2.1 SO_2 isotopologues samples

129 The isotopically enriched $^{32,33,34,36}SO_2$ gas samples were prepared from elemental ^{32}S, ^{33}S, ^{34}S,
130 and ^{36}S powder (Isoflex USA) sealed with CuO in quartz tubes under vacuum, heated at 950°C
131 for 15 min. Separation of SO_2 samples and unreacted O_2 was done by freeze-pump-thaw
132 cycling. The components of the gas phase labeled samples were confirmed and purified using
133 a GC-MS, and the products purity was checked by quantitative IR spectroscopy (Danielache et
134 al., 2012). Details of sample preservation are described in Endo et al. (2022a).

135 ### 2.2 Instrument setups

136 The gas cell and inlet gas system follows Endo et al. (2022a). The UV absorption cross-sections
137 were determined using a Fourier transform spectrometer (VERTEX 80v, Bruker, Japan) with
138 an external deuterium lamp (L6301-50, Hamamatsu, Japan) equipped at the inlet port on the
139 right spectrometer side. Two capacitance manometers (CMR362 and CMR364, Pfeiffer,
140 Germany) calibrated the pressure using a full-range gauge (PGE500, INFICON, Germany) and
141 local weather reports. An oil pump was added to the gas line system for pre-vacuuming to
142 extend the lifetime of the turbopump system (Pfeiffer, Germany).

143 Signal drifting from the light source was observed, where the signal intensity decreases over
144 time. Following a commonly used method (Danielache et al., 2008; Danielache et al., 2012;

Endo et al., 2022a; Vandaele et al., 2009), where the background signal intensity at the time of the sample signal measurement was derived by alternating the background and sample signal measurements and calculating the average of the two background signal before and after each sample signal measurement.

Numerous measurement parameters were adjusted to balance high-resolution and relatively low noise levels while limiting the measurement time to avoid excessive errors brought by signal drift. The interferogram from a single measurement was derived from an average of 150 scans at a resolution of 0.4 cm^{-1} using single-sided and bi-directional acquisition mode and was converted to signal intensity spectrum by Fourier transform using boxcar apodization function and Mertz phase correction mode to preserve the most original data possible. A frequency window from 0 to 60,000 cm^{-1} and a zero-filling number of 2 produced a spectrum ranging from 41666 to 29400 cm^{-1} with a data point spacing of ca. 0.12055 cm^{-1}. No prominent peaks spread due to the grazing-incidence light in the UV region measurement was observed, and an 8 mm aperture size was selected. The VERTEX 80v instrument used in our measurements is capable of a maximum spectral resolution of 0.1 cm^{-1}. However, the optimal trade-off between spectral resolution and spectral noise was found to be 0.4 cm^{-1} which is between 5 to 10 times lower in resolving power than the suggested optimal spectral resolution (Rufus et al., 2003).

2.3 Measurements

The Beer-Lambert law,

$$A = \ln\frac{I_0}{I} = \ln\frac{1}{Trans} = \sigma l \rho \tag{1}$$

Shows that absorbance A is proportional to attenuating number density of the gas sample ρ (in this report approximated as gas pressure, assuming a constant temperature). The radiant power intensity is reduced from I_0 to I, $Trans$ is the transmittance, σ is the absorption cross-sections, and l is the optical path length. Both logarithm and natural logarithm definition formats of absorbance are widely used. Which format is used does not affect the $A \propto C$ relationship, we used the natural logarithm format for a more convenient calculation of cross-sections. In this report, SO_2 absorption cross-section (σ) at each wavelength (λ) was calculated through the application of the Beer-Lambert law,

$$\sigma(\lambda) = -\frac{RT}{PN_A z}\ln\frac{2I(\lambda)}{I_{0a}(\lambda) + I_{0b}(\lambda)} = -\frac{1}{\rho z}\ln\frac{I(\lambda)}{I_{0ave}(\lambda)} = -\frac{1}{\rho z}\ln Trans(\lambda) \tag{2}$$

Where R is the gas constant, T is the room temperature in the laboratory, P is the sample pressure during measurement, N_A is the Avogadro number, z is the sample cell length (10.0 cm) through which the light passes, I is the measured sample signal intensity, I_{0a} and I_{0b} are the measured background signal intensity before and after a single sample measurement as mentioned above, and I_{0ave} is the mean signal intensity of I_{0a} and I_{0b}, Substituting (1) into (2) yields the following,

$$\sigma(\lambda) = -\frac{RT}{PN_A z}\ln T(\lambda) = k_1 \cdot \frac{A(\lambda)}{P} \quad (3)$$

Where $k_1 = \frac{RT}{N_A z}$, and

$$\sigma(\lambda) = -\frac{RT}{PN_A z}\ln T(\lambda) = k_2 \cdot TA(\lambda) \quad (4)$$

Where $k_2 = \frac{R}{PN_A z}$.

Equations **(3)** and **(4)** indicate that when σ is either pressure or temperature dependent, the linear relationship between A and P is not valid. In this study, the temperature is assumed to be constant since variability was within a range of a few digress. The measured data showed no pressure-dependent cross-sections. **Figure 1** shows the relation between sample pressure in the gas cell and measured absorption-cross sections. Previous absorption cross-section measurements of various gas and liquid species have acknowledged deviations from the Beer-Lambert law, that is an apparent cross-section pressure dependency (e.g., Kostkowski and Bass, 1956; Anderson and Griffiths, 1975; Mellqvist and Rosén, 1996; Endo et al., 2015; Li et al., 2022).In both reports the origin of such non-linear behavior is attributed to low spectral resolution of the instrument. The data presented in this report, which was recorded at spectral resolution of 0.4 cm^{-1}, shows no apparent pressure-dependent cross-section variability (**Figure 1**). Thus, it is not required to correct the apparent cross-section pressure dependency.

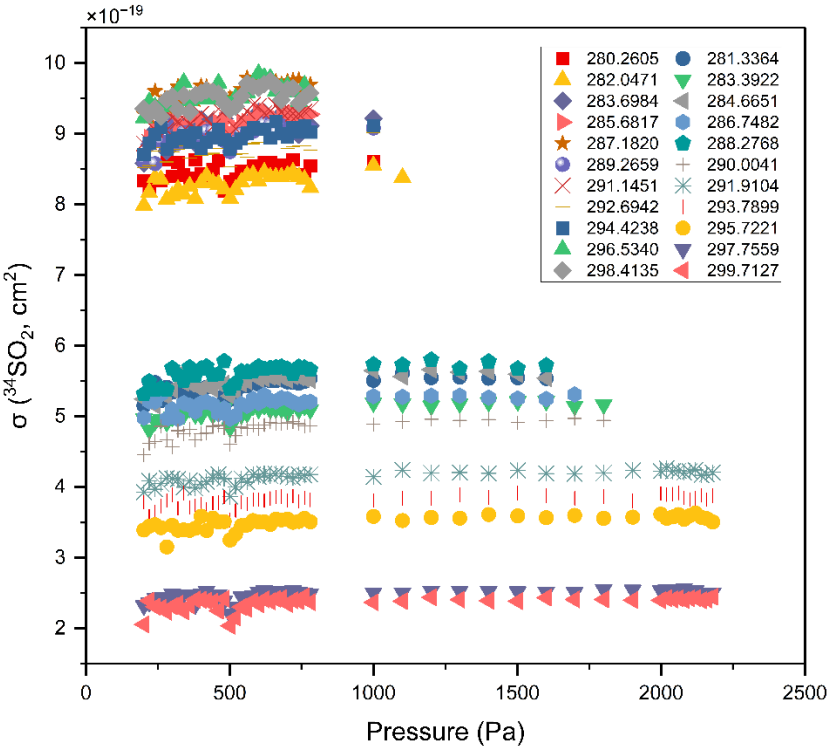

198 **Figure 1**: Individual cross-section data of each peak and valley at different pressures from
199 280−300 nm for $^{34}SO_2$. The $^{34}SO_2$ pressure ranges from 200−2200 Pa. No apparent pressure-
200 dependent cross-section phenomenon was observed.
201

202 In actual measurements, many sources of uncertainty can affect the linear relationship between
203 A and P. In the case of a high-precision Fourier transform spectrometer, the dark current and
204 amplifier noise from regions where source intensity and detector sensitivity are low, the photon
205 detector shot noise, the cell positioning uncertainties, etc., making different orders of impact
206 on the relative signal intensity uncertainty (Skoog et al., 2017). These random noises are almost
207 impossible to distinguish from each other thoroughly. Common solutions include averaging
208 multiple sets of measurements (Blackie et al., 2011; Rufus et al., 2003; Stark et al., 1999;
209 Vandaele et al., 2009), adding weights to the parameters that characterize the data (Danielache
210 et al., 2008; Danielache et al., 2012), and calibration of SO_2 column density dependence on
211 measured cross-sections with a least squares method (Endo et al., 2015). Nonetheless,
212 conventional methods still do not resolve the bias that noise from different sources introduce
213 to the actual absorptivity.

214 In this study, we implemented a linear regression technique to rule out the effect of random
215 noise. The LAD method was deployed to clarify the linear relationship between A and P,
216 following the purpose of minimizing the sum of the absolute values of the residuals S between
217 raw data y_i to the fitted data $f(x_i)$,

218 $$\text{argmin } S = \sum_{i=1}^{n} |y_i - f(x_i)| \tag{5}$$

219 A universal algorithm from the Scikit-Learn machine learning library (Pedregosa et al., 2011)
220 for the Python programming language was used for computational efficiency considerations.
221 Based on the degree of data dispersion, scenarios that linear regression needs to target can be
222 categorized into three. Case 1: Little effect of random noise on the data, where A and P have
223 good linear fit, and there is little difference compared to the commonly used least squares (LS)
224 linear regression. Case 2: The effect of random noise on individual data creates outliers, and
225 the LAD method excludes the impact from outliers much better than the LS method. Case 3:
226 Highly discrete data in high noise regions, the linear relationship between A and P is almost
227 indistinguishable, and all current methods do not guarantee noise removal.

228 The number of valid measurements at a given wavelength used in the LAD linear regression
229 ranged between 10 and 70 depending on signal-to-noise and the amount of available sample
230 (**Figure S2)**. The increased number of measurements are a necessary condition for reducing
231 the errors associated with signal-to-noise issues. Previous measurements on isotopic effects of
232 ultraviolet absorption cross sections reported by the authors (Danielache et al., 2008, 2012;
233 Hattori et al., 2011; Endo et al., 2015, 2022a) have been aware of this issue but limitations on
234 sample and instrument accessibility have limited the number of measurements. In this report
235 the number of measurements were increased to a number where an analysis of the limit of noise
236 reduction by number pf measurements was conducted. At least 10 measurements are required

to reduce the LAD algorithm error. 15−25 sets of measurements are recommended, and the improvement in error is no longer apparent after more than 30 sets.

With the above reference parameters, the final cross-sections are calculated as follows. Firstly, the collected raw data were prefiltered to retain the data with transmittance from 0.1 to 0.95, which not only excluded the data with too low signal intensity but also the transmittance range was chosen to consider the effect of instrument noise on the measurement precision (Skoog et al., 2017). Next, data with signal-to-noise ratio (SNR) less than 20 were excluded to further improve data quality. The filtered data are involved in the following data correction of the linear relationship between A and P by the LAD method. Finally, the corrected A allows the calculation of the cross-sections at the corresponding wavelength.

2.4 Error budgets

The errors in this study came mainly from four main sources. (1) The temperature variation of the experimental environment was within 2.5 K, introducing an error of 0.85% to the final cross-sections. (2) The mechanical error of the pressure gauge, according to the manufacturer's instructions, has a validity of about 0.2%. (3) Each measurement took about 20 min, and the pressure change due to SO_2 adsorption to the sample cell and stainless tube wall introduced an error of about 0.2%. (4) The errors from instrumental random noises are mostly reflected in the dispersion of the linear relationship between A and P, following,

$$S_{y/x} = \sqrt{\frac{\sum\left(y_i - f(x_i)\right)^2}{n-2}} \tag{6}$$

3 Results and discussions

3.1 Comparisons with previous studies

The measured $^{32}SO_2$ absorption spectrum in the present study is compared to four previous studies on SO_2 in the $\tilde{B}^1B_1$-$\tilde{X}^1A_1$ absorption band (**Figure 2**) and spectral summary listed in **Table 1**. There are two previous studies about the SO_2 isotopologues with spectral resolution of 25 cm^{-1} (Danielache et al., 2008) and 8 cm^{-1} (Danielache et al., 2012) and errors of 1.2−2.5% and 1.2−8.2% respectively. For comparison, two naturally abundant SO_2 studies with high resolution are presented. The study from Vandaele et al. (2009) with spectral resolution of 2 cm^{-1} and 4−6% error. A high-resolution natural abundance measurement from Rufus et al. (2003) with spectral resolution of 0.04−0.13 cm^{-1} resolution and 5% error. This study improves the spectral resolution of the existing isotopic spectrum by a factor of 20, while the error in the 260−300 nm band is comparable to spectra of natural abundance at about ten times higher resolution.

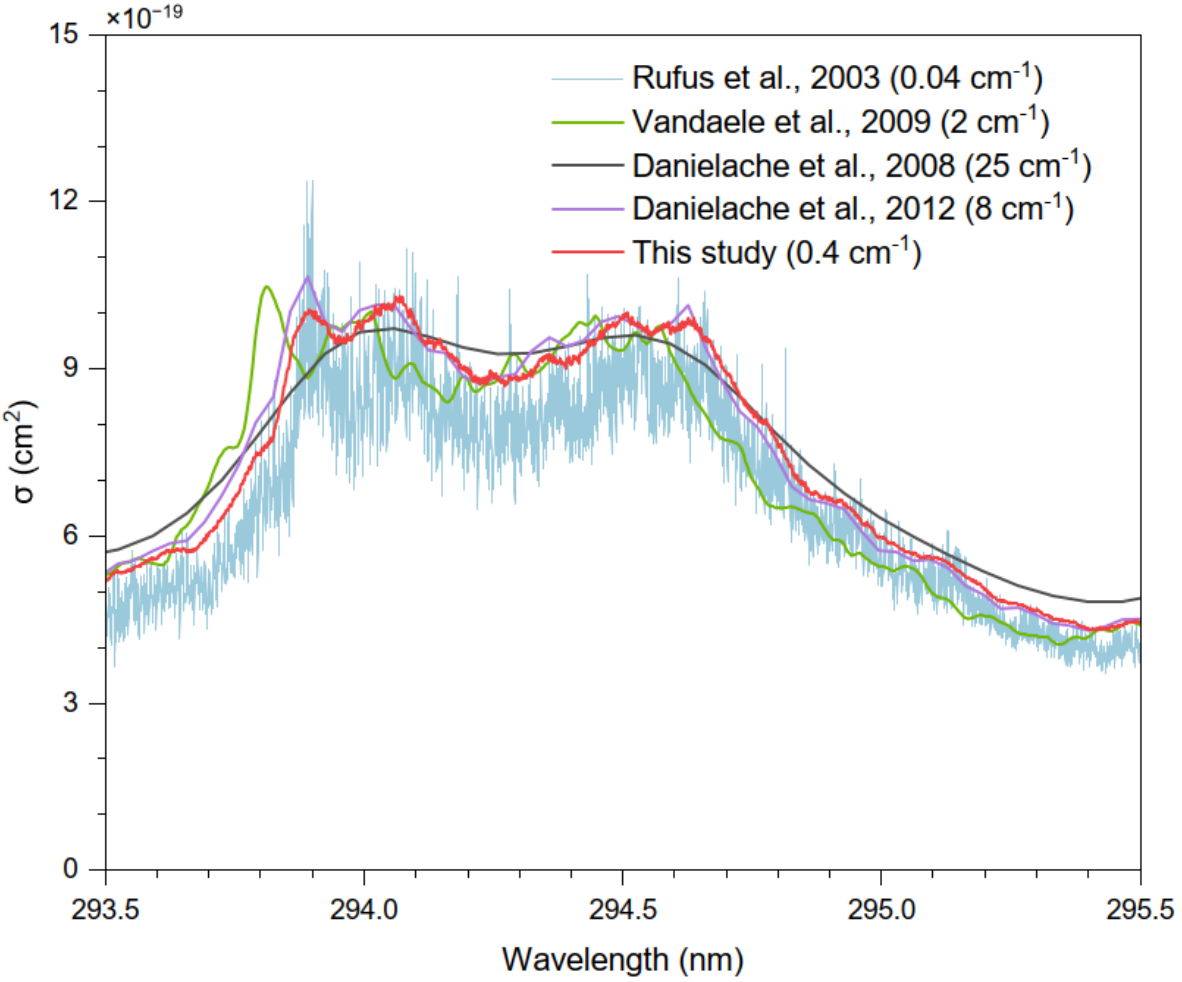

Figure 2: Comparison of measured $^{32}SO_2$ absorption spectrum in this study with spectra reported by Rufus et al. (2003), Vandaele et al. (2009), Danielache et al. (2008) ($^{32}SO_2$, 25 cm^{-1}), and Danielache et al. (2012) at the 293.5−295.5 nm spectral range. All the reported spectra were measured at room temperature (293−298 K) therefore spectral differences are not expected to be produced by temperature differences. Spectra reported by Rufus et al. (2003), Vandaele et al. (2009) are for natural abundance SO_2 samples. $^{32}SO_2$ spectrum data in Danielache et al. (2008) used natural abundance samples and calibrated with measured $^{33}SO_2$ and $^{34}SO_2$ spectra. Spectra in this report and Danielache et al., (2008) are from isotopically enriched $^{32}SO_2$ samples.

Table 1: Summary and comparison of studies on SO_2 absorption b-band.

Reference	Isotope	Resolution (cm^{-1})	Average Error (%)	Temperature (K)
Present study	$^{32,33,34,36}S$	0.4	~5.1($^{32}SO_2$) ~4.0($^{33}SO_2$) ~4.5($^{34}SO_2$) ~4.1($^{36}SO_2$)	293

Rufus et al. (2003)	Natural abundance	0.04-0.13	~5	295
Vandaele et al. (2009)	Natural abundance	2	~4-6	298
Danielache et al. (2012)	^{32,33,34,36}S	8	~2.2($^{32}SO_2$) ~1.8($^{33}SO_2$) ~1.2($^{34}SO_2$) ~2.5($^{36}SO_2$)	293
Danielache et al. (2008)	$^{Nat.,33,34}$S	25	~1.2(Nat.) ~3.8($^{33}SO_2$) ~8.2($^{34}SO_2$)	293

Note. Comparison of peaks at different resolutions show that the spectrum in this study exhibits significantly better peak separation than the low-resolution studies (Danielache et al., 2008; Danielache et al., 2012; Vandaele et al., 2009). Even the spectrum from Vandaele et al. (2009), which has only a five-times difference in resolution, can observe much more resolved peaks. This study also shows excellent control of baseline noise, which is about the same as the lower resolution spectrums compared to the ten times higher resolution spectrum from Rufus et al. (2003). The peak position in this study fits the result from Danielache et al. (2012), while the spectrum from Danielache et al. (2008) is unsuitable for comparison due to band shape distortion by low resolution. The peak position in the spectrum from Vandaele et al. (2009) shows a slightly blue shift compared to the spectrum from Rufus et al. (2003), which is also of natural abundance.

The cross-sections calculated using the LAD method are also compared to those calculated using the averaging method as illustrated in **Figure 3**. The new LAD method perfectly reproduces the peak positions and peak intensities derived from the averaging method over the entire measurement band. From **Figure 3 (b)**, it can be concluded that the subtle differences between the two methods are mainly reflected in the position of the spectral peaks, and the magnitude of the difference increases with the intensity of the peaks. **Figure 3 (c)** shows that the difference is about 10^{-2} of the intensity of the cross-sections, and there is a relatively high difference of about 2-3% at the low SNR positions at both ends of the measurement band, and about 1% at the high SNR positions in the middle of the measurement band. The comparison of errors between two methods are shown in **Figure 4**, where the spectral data of $^{32}SO_2$ measured in this study are used. The error calculation of averaging method follows Stark et al. (1999) that includes uncertainty in the absorbing column density N of SO_2, uncertainties in the values of $I(\lambda)$ and $I_{ave}(\lambda)$ associated with the measurement SNR for $I_{0ave}(\lambda)$, and the systematic errors associated with inadequate spectral resolution, following,

$$\frac{\Delta\sigma}{\sigma} = \left[\left(\frac{\Delta N}{N}\right)^2 + \left(\frac{1}{(SNR)N\sigma}\right)^2 \{1 + e^{2N\sigma}\}\right]^{0.5} \quad (7)$$

The averaging method shows higher error than the LAD method, with 20-40% error in low SNR regions at both ends of the measurement band range and 10% in high SNR regions. The mean error for the averaging method is 15.1% in the 240-320 nm band range, compared with the 5.1% error using the LAD method, indicating the new algorithm reduces the error by a factor of about three. Since the LAD method does not require separating multiple sources of

noise and calculating the errors brought by each type of noise individually, it treats them as a whole and discriminates the errors by the dispersion of the linear relationship between absorbance and gas pressure, as well as introducing a sufficiently large number of measurement groups to improve the reliability of the data.

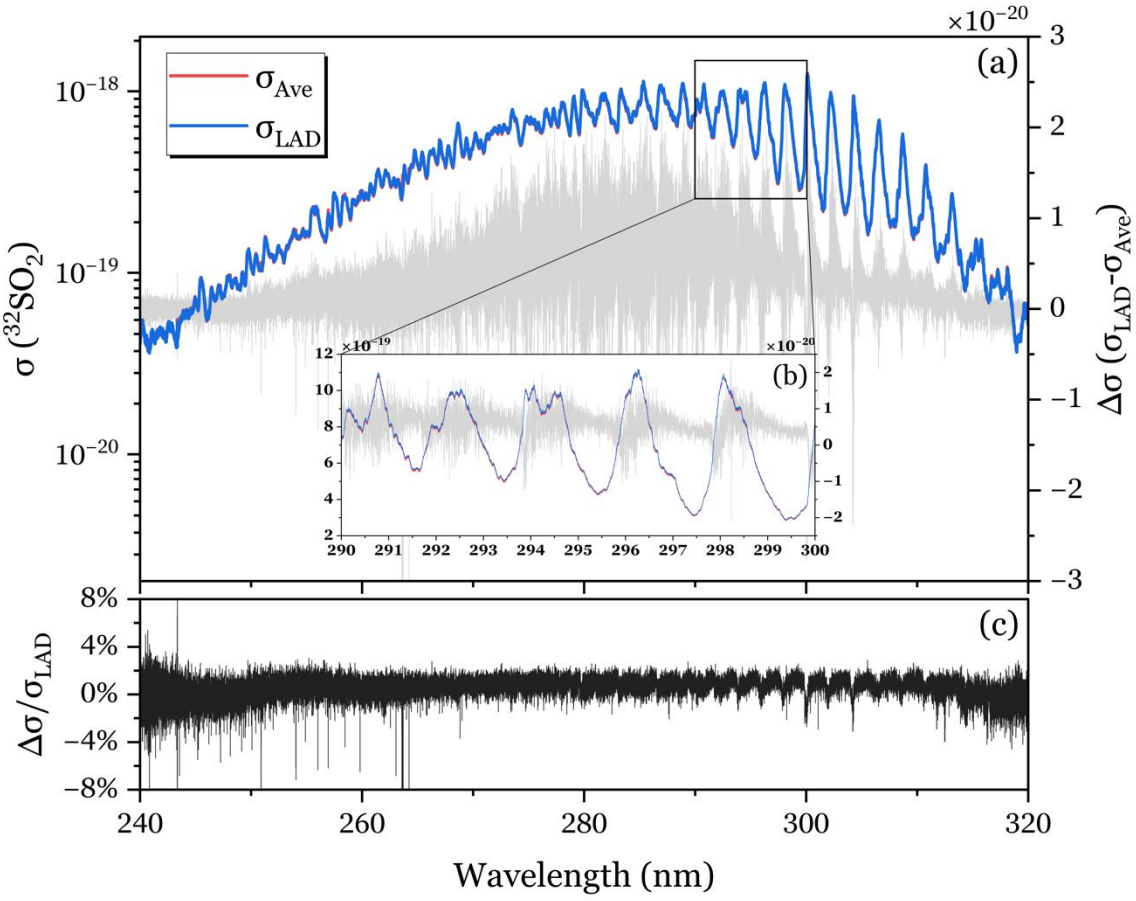

Figure 3: Comparison of spectra obtained the LAD and averaging methods (panel a), and difference between both methods grey color line for the 240−320 nm spectral range. Panel (b) shows an enlarged comparison for the 290−300 nm spectral range. Panel (c) shows the relative of difference between the two methods respect to the spectrum obtained by the LAD method. From the panel c can be seen that both methods yield spectra with a maximum difference of c.a. ±4%.

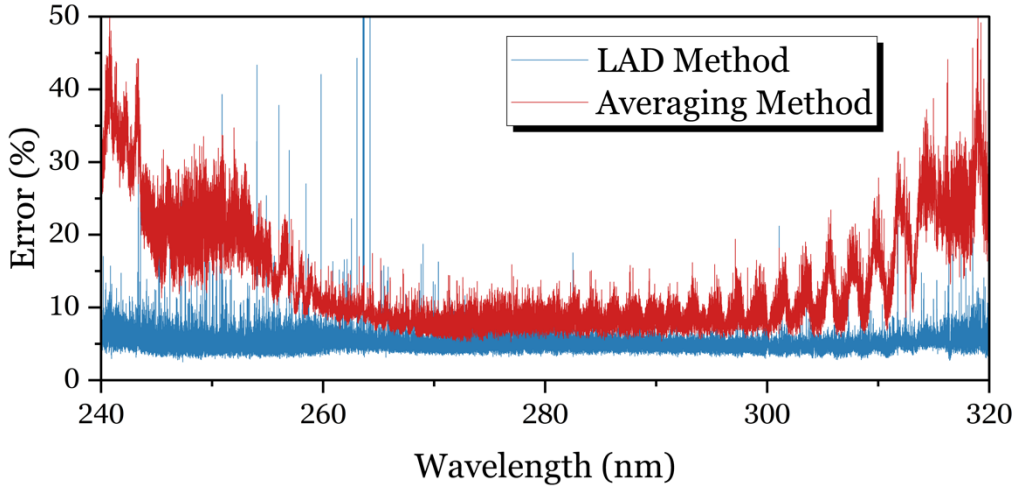

Figure 4: Error comparison between the LAD method and the averaging method for the spectral data of $^{32}SO_2$ measured in this study. The error calculation of the averaging method follows Stark et al. (1999) that includes the uncertainty in the column density, the uncertainties in the value of $I(\lambda)$ and $I_{0ave}(\lambda)$ associated with the measurement SNR for $I_{0ave}(\lambda)$, and the systematic errors associated with inadequate spectral resolution.

3.2 Isotopic Fractionation in SO_2 Photoexcitation

The measured absorption cross-sections are shown in **Figure 5**, where values of σ for $^{32,33,34}SO_2$ at 240−320 nm were successfully measured. However, due to insufficient samples as illustrated in **Figure S3**, $^{36}SO_2$ in the 240−245 nm band could not be measured. The errors in the measured cross-sections are in the range of 3−10% shown in **Figure 6**, with relatively high errors in the 240−260 nm and 310−320 nm bands.

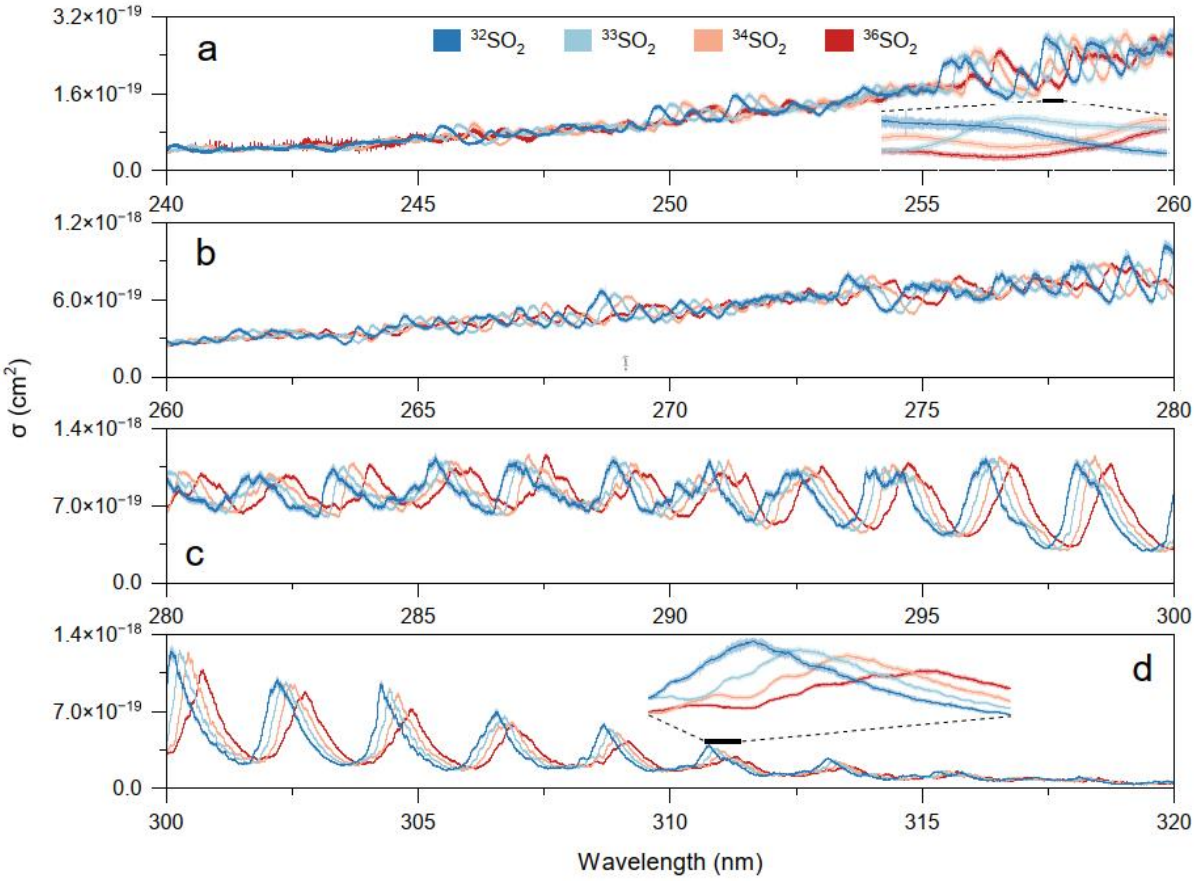

Figure 5: Measured absorption cross-sections of $^{32}SO_2$, $^{33}SO_2$, $^{34}SO_2$, and $^{36}SO_2$, absorption cross-sections and estimated errors. For clarity panels a,b,c and d divide the spectrum in four spectral ranges 240−260nm, 260−280 nm, 280−300 nm and 300−320 nm respectively. Sub-sets in panels a and d show an expanded fraction of the spectra to make more readable the associated error bars to each wavelength. As the mass of the 13sotopologues increases a significant redshift in the position of the peak of the absorption spectrum can be observed starting at the spectral band origin near 317 nm.

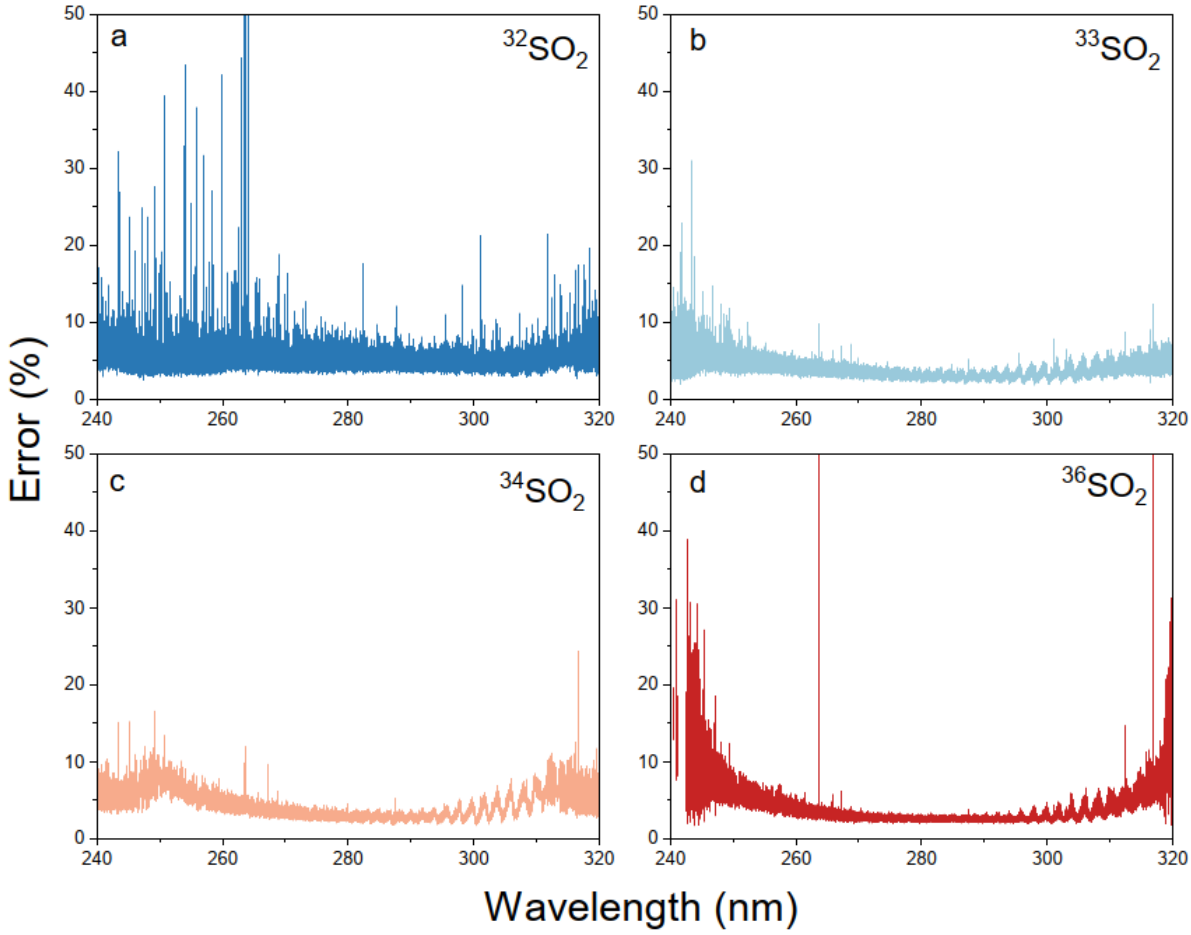

Figure 6: Relative error of $^{32}SO_2$, $^{33}SO_2$, $^{34}SO_2$, and $^{36}SO_2$ respect to measured absorption cross-sections. Lack of precision due to insufficient signal-to-noise ratio is more pronounced at edges of the measurement spectral band.

The redshift of the SO_2 rare isotopologues relative to $^{32}SO_2$ at each peak position is more pronounced for heavier isotopes. The wavelength-dependent isotopic fractionation constant $^{3x}\varepsilon(\lambda)$ was calculated to describe the isotopic effect (Ueno et al., 2009), following,

$$^{3x}\varepsilon(\lambda) = 1000 \times \ln\left[\frac{\sigma^{3x}SO_2(\lambda)}{\sigma^{32}SO_2(\lambda)}\right] [‰] \quad (8)$$

where $\sigma^{3x}(\lambda)$ is the absorption cross-section for a given 14sotopologues (^{3x}S, namely ^{32}S, ^{33}S, ^{34}S, or ^{36}S) at wavelength λ. The result is shown in **Figure 7**, this study extends the existing value of fractionation constant by 10 nm at shorter wavelengths compared to the previous study (Danielache et al., 2012). The peak positions in the highly structured absorption cross-sections are consistent with Danielache et al. (2012), but the values at both ends of the measurement band are slightly smaller.

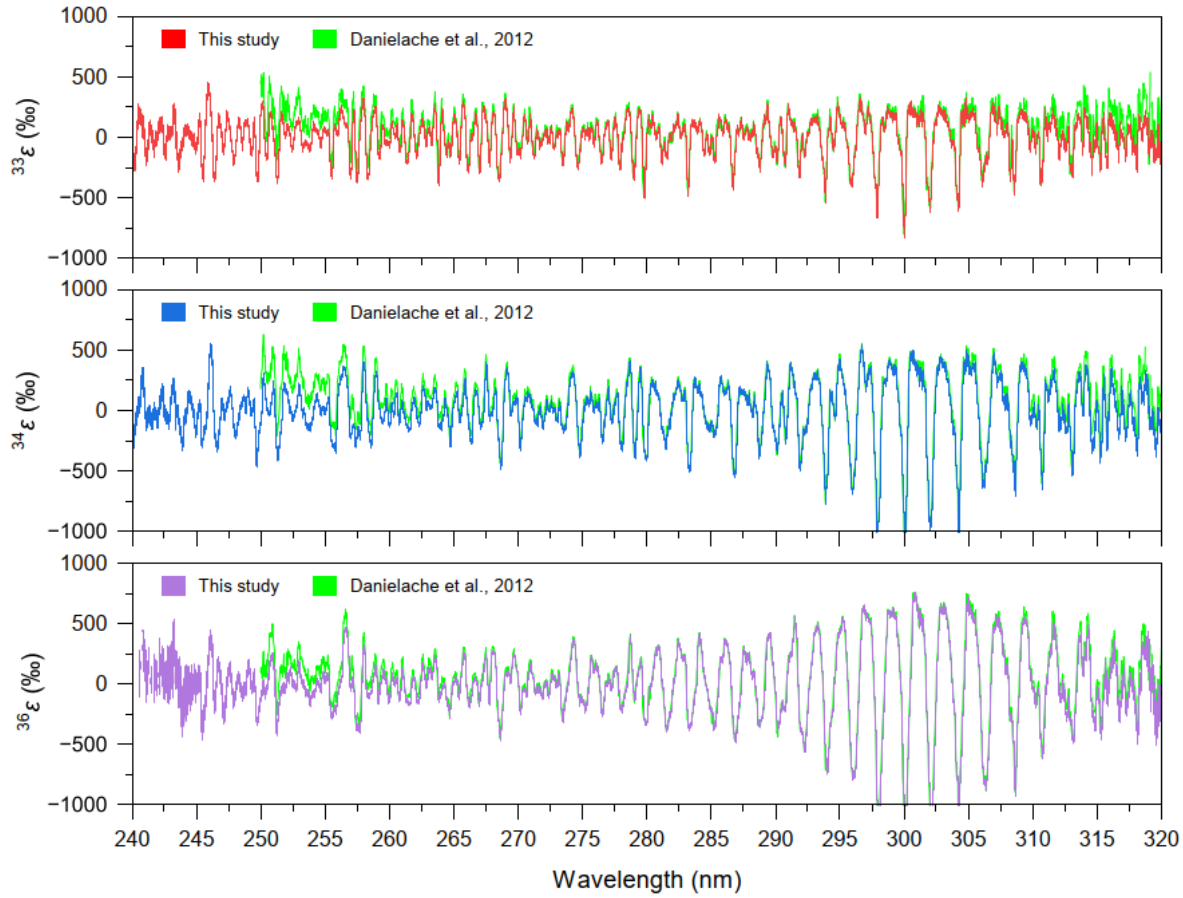

Figure 7: Fractionation constant of $^{33,34,36}\varepsilon$ as a function of wavelength from measured absorption cross-sections ($^{3x}\varepsilon(\lambda)$) compared to the previous study (Danielache et al., 2012). Newly reported spectra show a large wavelength specific isotopic effect which are similar to previously reported spectra. Significant differences can be seen at edges of the measured spectra in the ~250 nm and ~315 nm region.

The magnitudes of S-MIF for the four stable sulfur isotopologues are given by the linear expressions as follows,

$$^{33}E_\lambda = {}^{33}\varepsilon_\lambda - 0.515 \times {}^{34}\varepsilon_\lambda \quad (9)$$

$$^{36}E_\lambda = {}^{33}\varepsilon_\lambda - 1.9 \times {}^{34}\varepsilon_\lambda \quad (10)$$

where the values 0.515 and 1.9 are the high-temperature limit values for the equilibrium partition function ratio for isotope exchange reactions (Hulston and Thode, 1965). As shown in **Figure 8**, the S-MIF constant of ^{33}E and ^{36}E largely agree to the previous study (Danielache et al., 2012), with the values at both ends of the measurement band are slightly deviated.

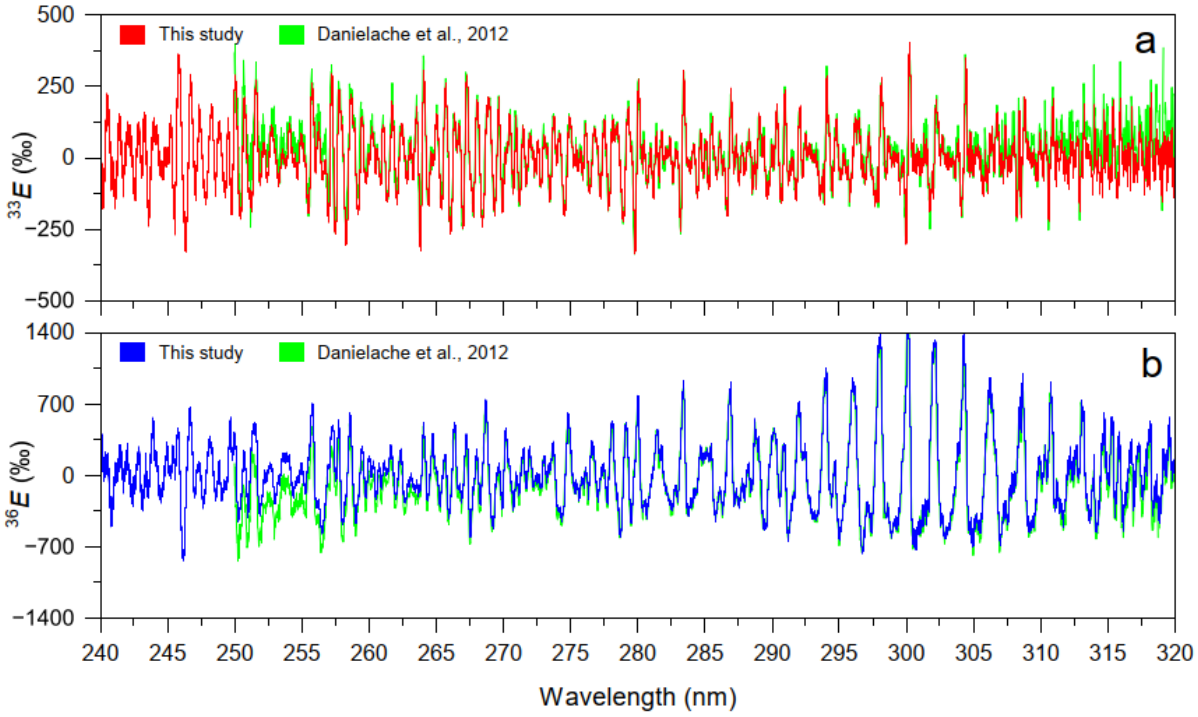

Figure 8: The Mass-independent fractionation constant ^{33}E and ^{36}E calculated from standard S-MIF values of 0.515 and 1.9 as a function of wavelength compared to Danielache et al. (2012). Newly reported spectra show a large wavelength specific isotopic effect which are similar to previously reported spectra. Significant differences can be seen at edges of the measured spectra in the ~250 nm and ~315 nm region.

Generally, $^{33,34,36}\varepsilon$ and ^{33,36}E mostly reproduced the results from the previous study (Danielache et al., 2012) regardless of the higher resolution of this report. The deviation at both ends of the measurement band could come from many factors, the largest of which is likely to be the low SNR brought about by insufficient background signal intensity.

The sulfur isotopic fractionation for SO_2 photodissociation in $\tilde{C}^1B_2$-$\tilde{X}^1A_1$ absorption band and photoexcitation in $\tilde{B}^1B_1$-$\tilde{X}^1A_1$ absorption band were also calculated. The photochemistry reaction rates for each sulfur 16sotopologues in the atmosphere follows,

$$^{3x}J = \int_{\lambda_0}^{\lambda_1} \Phi(\lambda) \cdot I(\lambda) \cdot {}^{3x}\sigma(\lambda)\, \mathrm{d}\lambda \tag{11}$$

Where Φ is the quantum yield (assumed as 1) and I is the actinic solar flux derived from Gueymard (2004). The S-MIF signatures $^{33,36}E$ of sulfur isotopes by SO_2 photochemical reactions are then calculated from ^{3x}J follow,

$$^{3x}\varepsilon = 1000 \ln \frac{^{3x}J}{^{32}J} [‰] \tag{12}$$

$$^{33}E = {}^{33}\varepsilon - 0.515 \times {}^{34}\varepsilon \quad (13)$$

$$^{36}E = {}^{36}\varepsilon - 1.9 \times {}^{34}\varepsilon \quad (14)$$

The errors derived from the LAD method produce a simple standard deviation which in this report is represented as σ ($\sigma^{3x}J$, $\sigma^{3x}\varepsilon$ and $\sigma^{3x}E$). For a detailed description on the error propagation procedure see the corresponding section in the additional information. Calculated ^{3x}J values from cross-sections obtained by the LAD and averaging methods are presented and compared in **Figure 9** and **Table 2**. As presented in **Figure 2a**, cross-sections obtained by both methods are almost identical and therefore the calculated ^{3x}J values are numerically similar. The propagated errors are significantly different where the robustness of the LAD method is reflected in the propagated $\sigma^{3x}J$ values which are roughly 2 orders of magnitude smaller to those obtained by the averaging method. The reduction of the calculated $\sigma^{3x}J$ values represent a breakthrough since they do not overlap with each other (**Figure 9** red and blue data sets) while the averaging method show significant overlap making the derived $\sigma^{3x}\varepsilon$ and $\sigma^{3x}E$ unreliable for geochemical predictions. The source in propagated error values can be traced to random errors produced by noise in the measured signal intensity (I or I_0 in Equation 1). Noise in the measured signal intensity I or I_0 for single measurements falls into the category of random errors. However, repeated measurements (See Figure S3 for the number reliable measurements at each wavelength and 17sotopologues) provide the necessary data required by the LAD method to systematically dismiss outlier data points produced by noisy conditions. The implementation of the LAD method reduces the random character of noise in the measured intensities to partially convert it into a systematic error. Calculated ^{3x}J values were compared to calculations under the same solar spectra for cross-sections reported by Danielache et al. (2008, 2012) measured at 25 cm^{-1} and 8 cm^{-1} numbers respectively. **Figure 10** compares these three data sets. One clear and counter intuitive trend is that the higher the spectral resolution the smaller the differences among ^{3x}J values. This trend has also been observed by Endo et al. (2015) for the $\tilde{C}$ - $\tilde{X}$ absorption band. The comparison is a clear reminder that when considering light induced isotopic effects predictions from single or a narrow band of wavelengths. Error bars for values measured at 8 cm^{-1} spectral resolution for ^{33}J and ^{34}J clearly overlap casting shadows on the reliability of the derived isotopic enrichment factors. The *J values* presented in this report present error bars which are far smaller than the *J values* themselves. Calculated $^{3x}\varepsilon$ and ^{3x}E are, as expected, similar in both methods while $\sigma^{3x}\varepsilon$ and $\sigma^{3x}E$ values obtained from the cross-sections calculated with the LAD are 1 order of magnitude smaller than those obtained by the averaging method (**Tables 3 and 4**).

Table 2. Calculated photoexcitation rate constants (^{3x}J) and propagated standard deviations ($\sigma^{3x}J$). All values are in molecules cm^{-3} s^{-1} units.

	^{32}J	^{33}J	^{34}J	^{36}J	$\sigma^{32}J$	$\sigma^{33}J$	$\sigma^{34}J$	$\sigma^{36}J$
LAD Method	3.0913×10^{-3}	3.0982×10^{-3}	3.1097×10^{-3}	3.1137×10^{-3}	7.03×10^{-7}	4.41×10^{-7}	4.42×10^{-7}	3.96×10^{-7}
Averaging Method	3.090×10^{-3}	3.097×10^{-3}	3.108×10^{-3}	3.113×10^{-3}	1.42×10^{-5}	1.42×10^{-5}	1.44×10^{-5}	1.44×10^{-5}

Table 3. Calculated isotopic enrichment factors ($^{3x}\varepsilon$) during photoexcitation and propagated standard deviations ($\sigma^{3x}\varepsilon$). All values are in permil (‰) units.

	$^{33}\varepsilon$	$^{34}\varepsilon$	$^{36}\varepsilon$	$\sigma^{33}\varepsilon$	$\sigma^{34}\varepsilon$	$\sigma^{36}\varepsilon$
LAD Method	5.91	2.22	7.22	0.26	0.26	0.26
Averaging Method	5.84	2.13	7.29	6.51	6.49	6.52

Table 4. Calculated mass independent isotopic enrichment factors (^{3x}E) during photoexcitation and propagated standard deviations ($\sigma^{3x}E$). All values are in permil (‰) units.

	^{33}E	^{36}E	$\sigma^{33}E$	$\sigma^{36}E$
LAD Method	-0.83	-4.02	0.19	0.36
Averaging Method	-0.88	-3.81	5.64	10.76

The introduction of the LAD method has made possible the reduction of propagated error bars to a point where reliable geochemical predictions are possible. Spectral resolution has also been a topic of concern. Previous measurements by Danielache et al. (2008, 2012) carried out at a spectral resolution of 25 cm^{-1} and 8 cm^{-1} respectively, the relation between spectral resolution and predicted isotopic effect has been so far acknowledged but not properly addressed. A definite study on the quantitative relation between isotopic effect and spectral resolution is yet to be done. Rufus et al. (2003) reported absorption cross for this band at a spectral resolution between 0.04 cm^{-1} and 0.13 cm^{-1}, which is according with their assessment sufficient to resolve all natural line widths. For the measurements in this report the optimal trade-off between spectral resolution and spectral noise was set to 0.4 cm^{-1}. Based on recent reports on pressure broadening (Lyons et al., 2018) and line profile density (Kumar et al., 2015) suggest that a spectral resolution 0.4 cm^{-1} could be sufficient for the study of photochemical induced isotopic effects at about 1 atm of pressure.

The calculated $^{34,33,36}\varepsilon$ and $^{33,36}E$ (**Figure 11**) enrichment factors derived from this and previous measurements are compared respect to spectral resolution at each measurement. All ^{3x}J values were calculated for a top of the atmosphere with a solar flux reported by Gueymard (2004) and adjusted to the spectral resolution of this report. Danielache et al. (2008) first presented spectrum of $^{32,33,34}SO_2$ but used natural abundance SO_2 as ^{32}S 18sotopologues, and a spectral resolution ~25 cm^{-1}. These first measurements were conducted at the very early stages of this decade long enquiry, they were designed for the $\tilde{C}$ -$\tilde{X}$ absorption band and issues of spectral resolution were not properly taken into account. Danielache et al. (2012) later improved the sample preparation and conducted the measurements at a higher resolution data (~8 cm^{-1}), and higher S/N ratios achieving propagated small error bars. This study introduced a new algorithm to further reduce the errors associated with increased resolution and the number of measurements at each pressure were extended the statistical maximum. The comparison in **Figure 11** suggest, yet do not quantitively prove, that the higher the spectral resolution, the smaller the isotopic effect for all $^{34,33,36}\varepsilon$ and $^{33,36}E$ values.

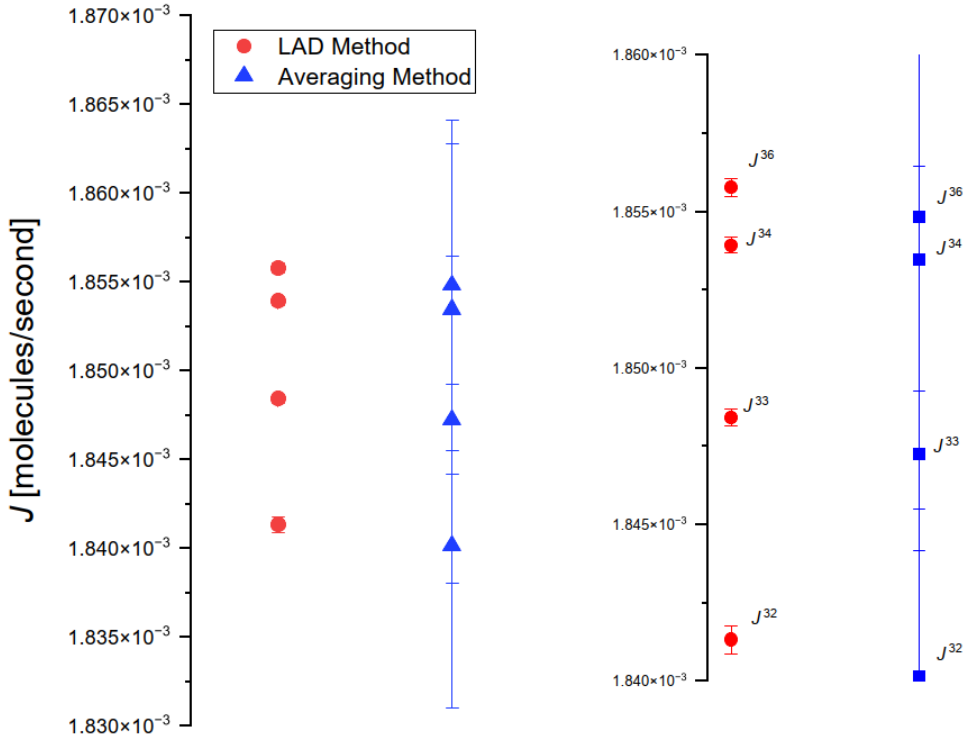

Figure 9: Photoexcitation rate constants calculated for a present Earth top of the atmosphere (TOA) conditions with actinic flux reported by (Gueymard, 2004)) for measured $^{32}SO_2$, $^{33}SO_2$, $^{34}SO_2$, and $^{36}SO_2$ isotopologues. The red and blue data sets represent cross-sections derived the LAD and averaging methods respectively. Both methods yield nearly the same *J* values. Propagated errors by the averaging method (red) produce error bars that overlap *J* values rendering them unreliable to geochemical predictions. The implemented LAD method (blue data sets) solves this problem.

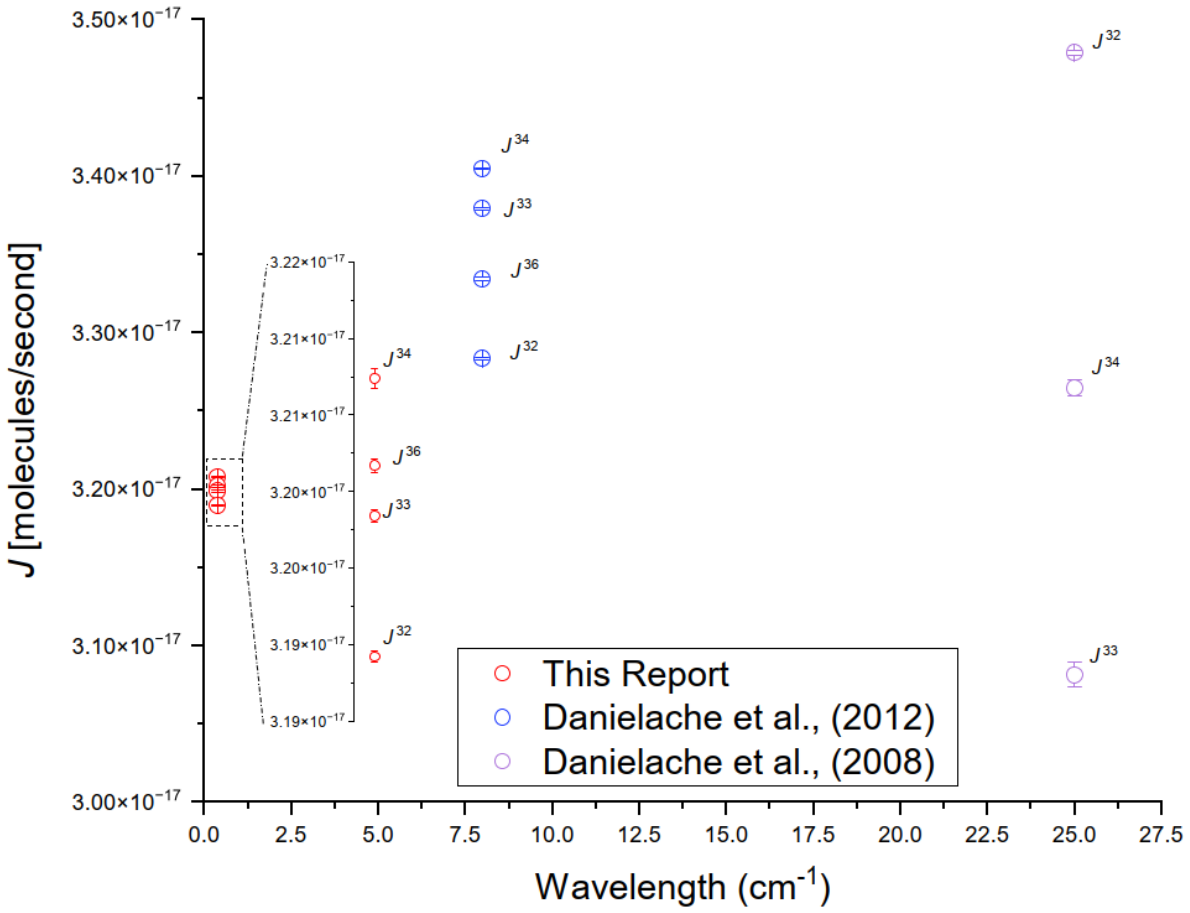

473

474 **Figure 10:** Photoexcitation rate constants calculated for a present Earth top of the atmosphere
475 (TOA) conditions with actinic flux reported by (Gueymard, 2004)) for measured $^{32,33,34}SO_2$
476 isotopologues and compared to previously reported by Danielache et al. (2008, 2012). The
477 newly reported data sets (black) have propagated error bars that are smaller than the differences
478 between calculated *J* values therefore making them reliable for geochemical predictions.

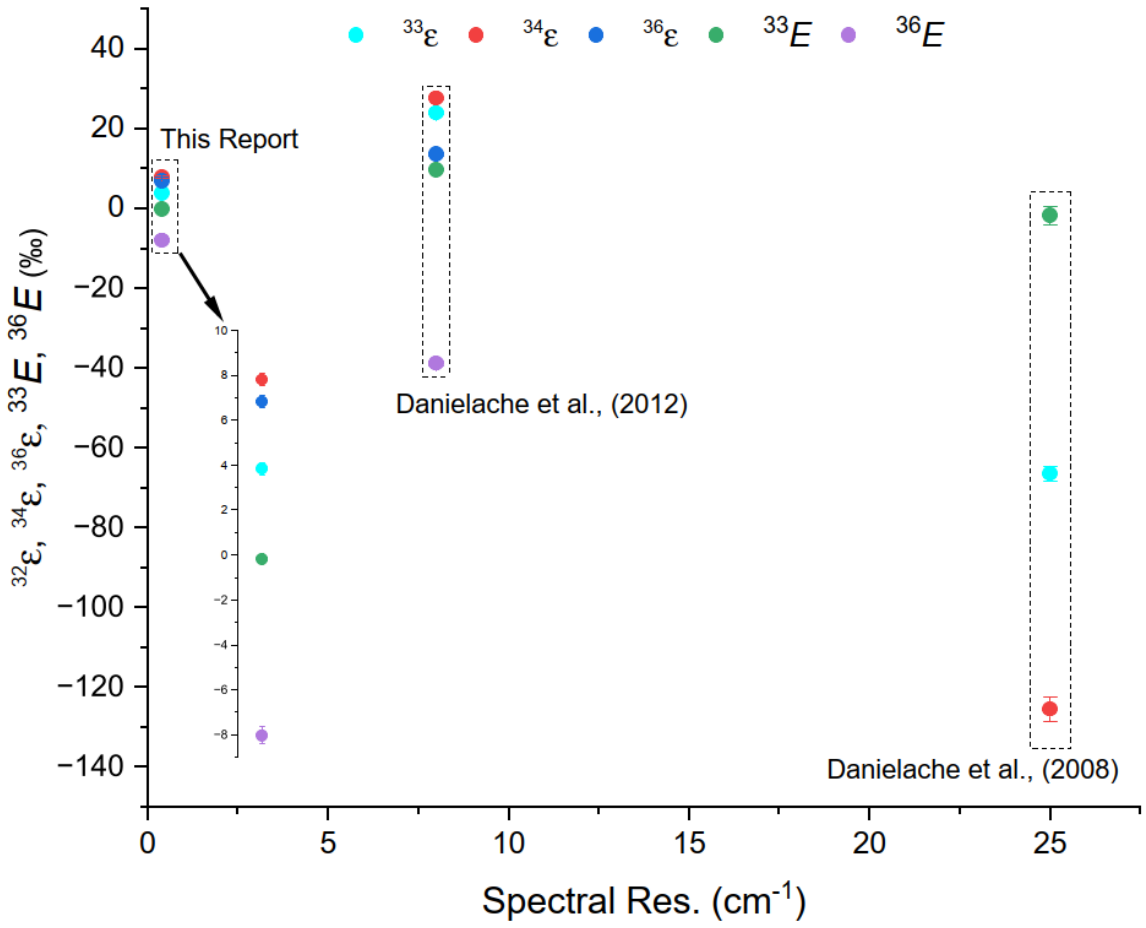

Figure 11: Relationship between isotopic fractionation $^{34,33,36}\varepsilon$ and $^{33,36}E$ vs. spectral resolution calculated from data in this report and compared to previously reported data by Danielache at al. (2008, 2012). The comparison of the data sets shows a clear trend where isotopic effects tend to be smaller with increased spectral resolution.

3.2 **Comparison with isotope fractionation observed in SO_2 photochemical experiments**

Sulfur isotope fractionation during SO_2 photoexcitation at wavelengths in the $\tilde{B}$ -$\tilde{X}$ band was investigated by UV irradiating SO_2 with natural isotope ratios and examining the sulfur isotope ratios of the products (referred to as SO_2 photochemical experiments below) (Endo et al., 2016; Whitehill and Ono, 2012; Whitehill et al., 2013)). Quadruple sulfur isotope analysis of the products show large S-MIF, with $\Delta^{33}S$ up to 78‰ (Whitehill et al., 2013) and up to 142‰ (Endo et al., 2016) with positive $\Delta^{36}S/\Delta^{36}S$ ratios. In this section, we compare isotope fractionation factors predicted from our absorption cross-section measurements with those previously observed in SO_2 photochemical experiments. Then, we discuss the origin of S-MIF, which occurs in SO_2 photoexcitation or related to the reaction.

Whitehill et al. (2013)) irradiated SO_2 with UV light under N_2 bath gas and measured quadruple sulfur isotopes of produced organics. They used a Xe arc lamp as a broadband UV source and controlled UV spectra with UV filters to prevent SO_2 photolysis and examine the wavelength dependence of the isotope fractionations. Acetylene was added as an electron donor in the

499 experiments. Although reactions are not fully understood, some organic sulfur matter was
500 produced and collected after UV irradiation. The expected relevant chemical pathways during
501 this experiment are reactions 1 to 4 (R1-R4) (e.g., Heicklen et al., 1980)

502 $$SO_2(^1A_1) + h\nu\ (240{-}320\ \text{nm}) \rightarrow SO_2(^1A_2\ v{=}n) + SO_2(^1B_1\ v{=}n)\ \text{(R1)}$$

503 $$SO_2(^1A_2\ v{=}n) + M \rightarrow SO_2(^1A_2\ v{=}0) + M\ \text{(R2)}$$

504 $$SO_2(^1A_2\ v{=}0) \rightarrow SO_2(^3B_1)\ \text{(R3)}$$

505 $$SO_2(^3B_1) + C_2H_2 \rightarrow \text{products (R4)}$$

506 The notation used in reactions 1 to 4 (R1 to R4) describe specific electronic and vibrational
507 states and are not frequent in chemical notation. Starting with R1 $SO_2(^1A_1)$ is the electronic
508 ground state with a given and unspecified rovibrational state. $SO_2(^1A_2\ v{=}n)$ and $SO_2(^1B_1\ v{=}n)$
509 are the photoexcited electronic $^1A_2/^1B_1$ manifold (mixing of two electronic states) at a given n
510 vibrational state (this fragment is also commonly known as SO_2*). In R2 M is a third body
511 collider (e.g., N_2) which triggers a quenching reaction to produce the electronic $^1A_2$ state at its
512 ground rovibrational state (v=0). R3 shows the intersystem crossing (ISC) from the singlet $^1A_2$
513 (v=0) state to the triplet ($^3B_1$). Because $SO_2(^3B_1)$ is more reactive than $SO_2(^1A_2/^1B_1)$ (Kroll et
514 al., 2018) $SO_2(^3B_1)$ reacts (R3) selectively with acetylene. The details of the reaction R4 have
515 yet to be understood, but they are unlikely to significantly contribute to S-MIF.

516 Isotopic fractionation factor in reaction R1 is predicted with absorption cross-sections of SO_2
517 isotopologues measured by this study and Danielache et al. (2012). Reactions other than
518 reaction R1 also may contribute to the isotopic fractionation observed in photochemical
519 experiments. Whitehill et al. (2013) suggested that reaction R2 mainly originated the observed
520 S-MIF in their experiments, mainly because (1) their theoretical study suggests that isotope
521 selective intersystem crossing might potentially contribute to the observed S-MIF and (2) their
522 results significantly differ from the S-MIF in reaction R1 predicted with SO_2 absorption cross-
523 sections measured by Danielache et al. (2012) (Fig. 13).

524 Furthermore, the observed MIF signature is considerably different from those predicted by
525 isotopologue-specific absorption cross-sections. They also show that excitation wavelength
526 range produces isotopic effects in the order of 20-60‰ for $\Delta^{36}S$ and 10-40‰ for $\Delta^{33}S$. The
527 wavelength range-isotopic effect is significant yet not as large as the pressure dependency
528 observed when the full spectral region of the $\tilde{A}^1A_2/\tilde{B}^1B_1$ manifold was photoexcited
529 (Whitehill et al., 2013, Fig. 2).

530 To compare our results with those of Whitehill et al. (2013), we calculate fractionation factors
531 using SO_2 absorption cross-sections of this study and Danielache et al. (2012) from Eqs. (11)
532 to (14), assuming a 150 W Xenon arc lamp spectrum and absorption spectra with UV filters.
533 The comparisons are shown in **Figures 12** and **13** where the isotopic effect produced during
534 the photoexcitation process (R1) is compared to the results from chamber experiments.

535 **Figure 12** compares $\Delta^{33}S$, ^{33}E values to $\delta^{34}S$, $^{34}\varepsilon$. The values reported by Whitehill et al. (2013),
536 regardless of excitation wavelength region or P_{SO2} do not match the ones calculated from the

537 spectra reported by Danielache et al. (2008) neither the ones calculated from the spectra in this
538 report. Large discrepancies are also observed on **Figure 13** where small and negative values of
539 ^{33}E and ^{36}E from spectra in this report show no correlation with large and positive $\Delta^{36}S$ and
540 $\Delta^{33}S$ isotopic ratios from the chamber experiments. Self-shielding calculations reported by
541 Whitehill et al. (2013) and photoexcitation induced enrichment factors calculated from data
542 reported by Danielache et al. (2008) and photoexcitation effects from the same spectra at
543 different spectral ranges independently calculated in this report, show large negative ^{36}E and
544 large positive ^{33}E values which don't match chamber experiments either.

545

546 From the comparisons in **Figures 12** and **13** the data presented in this report tend to support
547 the conclusions reported by Whitehill et al. (2013) that the MIF isotopic ratios measured in
548 collected organosulfur are likely produced by the ISC process in R3. Furthermore, the data in
549 this report in which values of $^{34}\varepsilon$, ^{33}E and ^{36}E being small and quite unsensitive to the excitation
550 wavelength band could contribute to the final organosulfur product MIF. This hypothesis does
551 not provide any explanation to the large $\Delta^{33}S$, $\Delta^{36}S$ values to $\delta^{34}S$ values reported from chamber
552 experiments under different band-pass filters, partial SO_2 and total N_2 pressures.

553

554

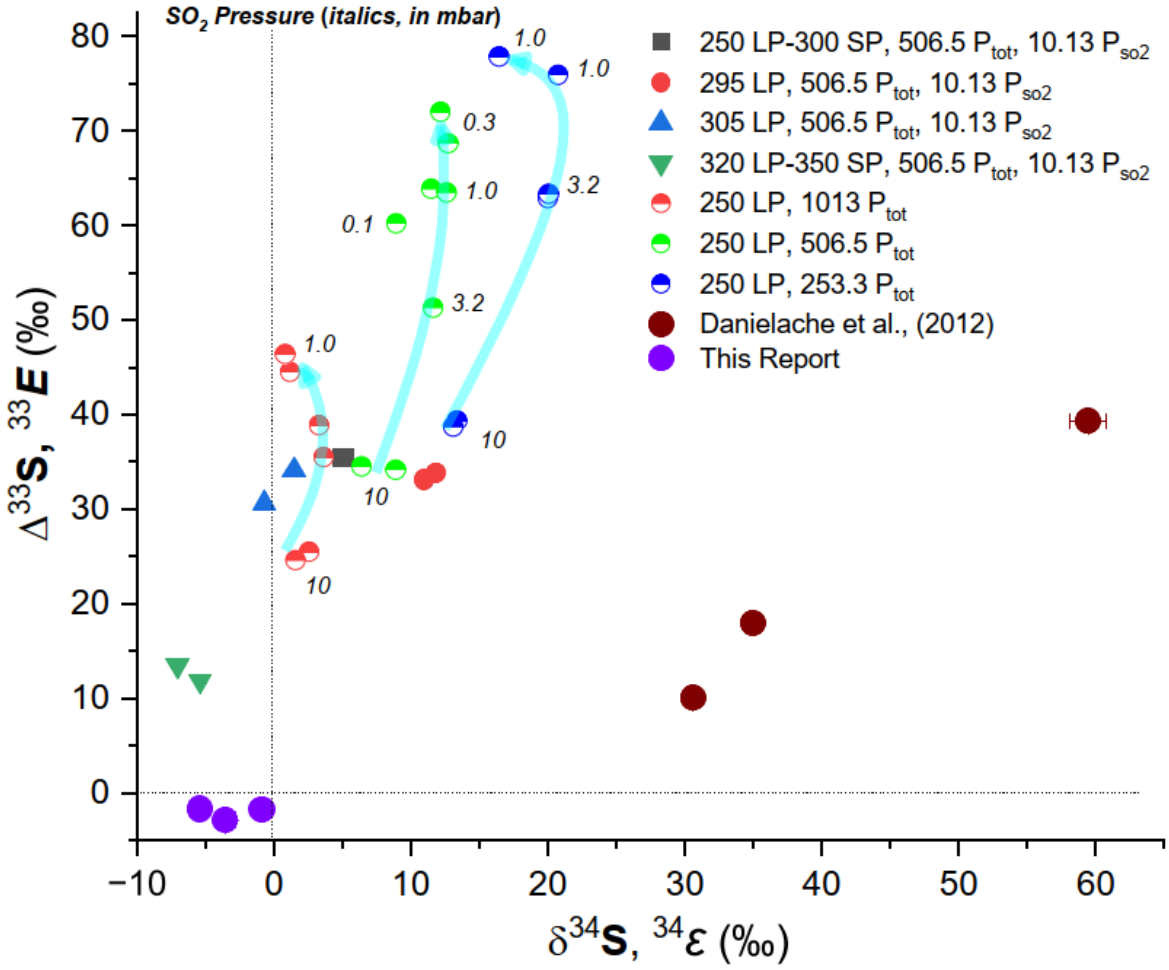

555

556 **Figure 12:** Calculated $^{34}\varepsilon$ vs. ^{33}E isotopic effects from spectra reported by Danielache et al.
557 (2012) and from spectra reported in this study using a 150W Xenon arc lamp spectrum and
558 compared to experiments by Whitehill et al. (2013)) ($\delta^{34}S$ and $\Delta^{33}S$). The units of the spectral
559 range are in nm, while P_{tot} (total gas pressures) and P_{SO2} (partial pressures of SO_2) are in mbar.
560

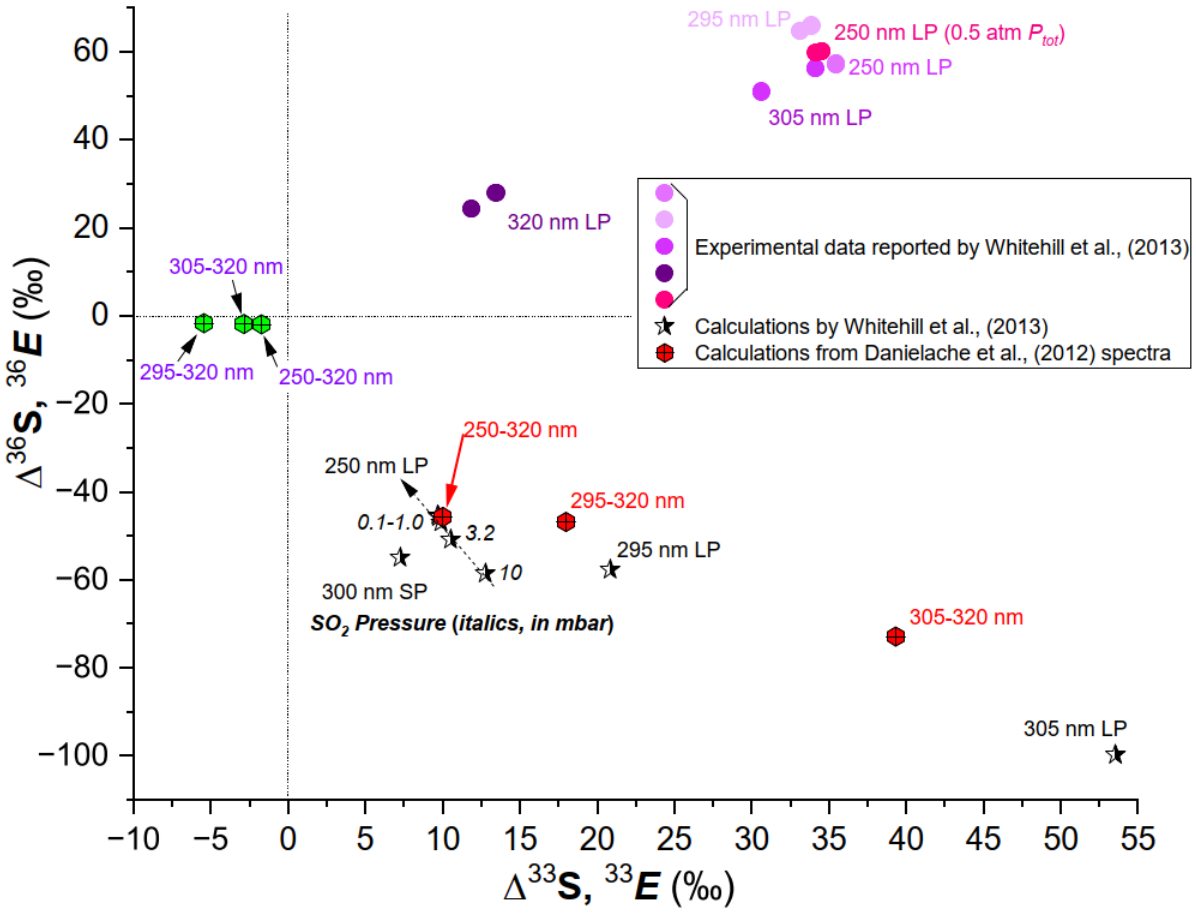

Figure 13: Calculated ^{33}E vs. ^{36}E isotopic effects from spectra reported by Danielache et al. (2012) and from spectra reported in this study using a 150W Xenon arc lamp spectrum and compared to experiments by Whitehill et al. (2013) ($\Delta^{33}S$ and $\Delta^{36}S$). P_{tot} (total gas pressures) and P_{SO2} (partial pressures of SO_2) are expressed in mbar units.

In order to assess the difference between the isotopic imprint between R1 and R3, next photoexcitation rate constants from isotopic-specific spectra in the 250−320 nm region were calculated and compared to chamber experiments reported by Whitehill and Ono (2012).

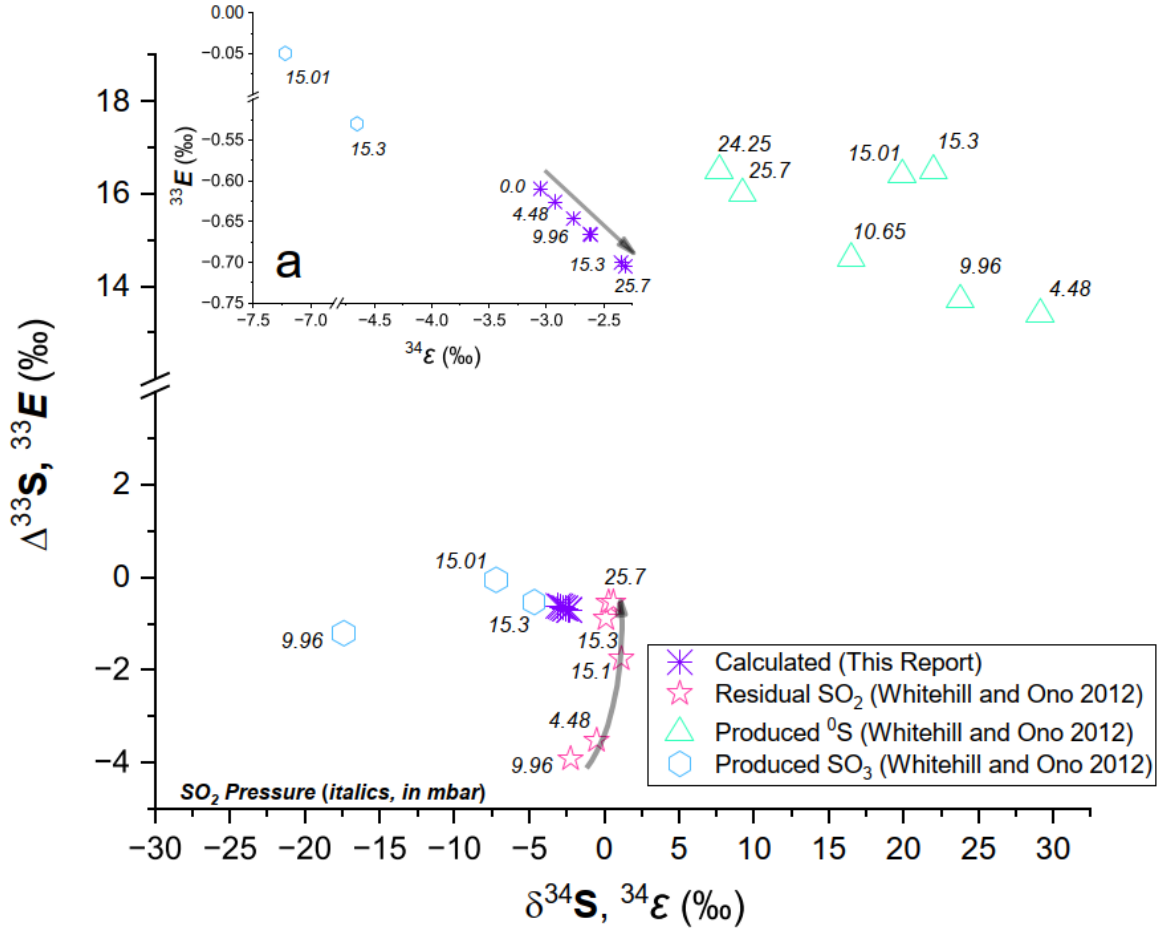

Figure 14: Calculated $^{34}\varepsilon$ vs. ^{33}E isotopic effects from spectra reported in this study using a 150W Xenon arc lamp spectrum and compared to experiments by Whitehill et al., 2013) ($\delta^{34}S$ and $\Delta^{33}S$).

Experiments conducted by Whitehill and Ono (2012) where they focused on isotopic mixing ratios ($\delta^{34}S$ vs. $\Delta^{33}S$ and $\Delta^{33}S$ vs. $\Delta^{36}S$) of oxydation products of photoexcited ($^1B_1$ $^1A_2$)SO_2 and residual ground state SO_2. For additional insight a simple self-shielded photoexcited enrichement factors ($^{34}\varepsilon$ vs. ^{33}E and ^{33}E vs. ^{36}E) at pressures ranging from 4.48 to 25.7 mbar using a 150W Xenon arc lamp spectrum was added to the analysis. The results are presented in **Figures 14** and **15**. **Figure 14** shows that calculated enrichment factors $^{34}\varepsilon$ and ^{33}E present clearly different values to isotopic mixing ratios $\delta^{34}S$ vs. $\Delta^{33}S$ for produced ^0S (Whitehill and Ono, 2012). Residual SO_2 show negative values of $\delta^{34}S$ and $\Delta^{33}S$, for experiments conducted at 25.7 mbar of partial pressure of SO_2, are quite similar to those calculated in this report. Most significantly, the calculated $^{34}\varepsilon$ and ^{33}E values are not only very close to those reported by Whitehill and Ono (2012) for produced SO_3, but they also have a very similar slope (inset **a**). The comparisons in **Figure 15** are even more revealing since ^{33}E vs. ^{36}E slope calculated from spectra in this report almost perfectly match the ^{33}E vs. ^{36}E slope reported by Whitehill and Ono (2012) for produced SO_3, and residual SO_2. Furthermore, in both cases the $^{36}E/^{33}E$ and $\Delta^{36}S/\Delta^{33}S$ slopes are particularly identical (**Figure 15** inset **a** for clarity). From the above discussion it can be suggested that the ($^1B_1$ $^1A_2$)SO_2 photoexcitation band is likely to have a

small isotopic effect that is transported to the SO_3 products. A quantitative mass balance analysis of the reaction products and residuals is necessary for obtaining further insight into the processes taking place at the chamber experiments reported by Whitehill and Ono (2012) and Whitehill et al. (2013).

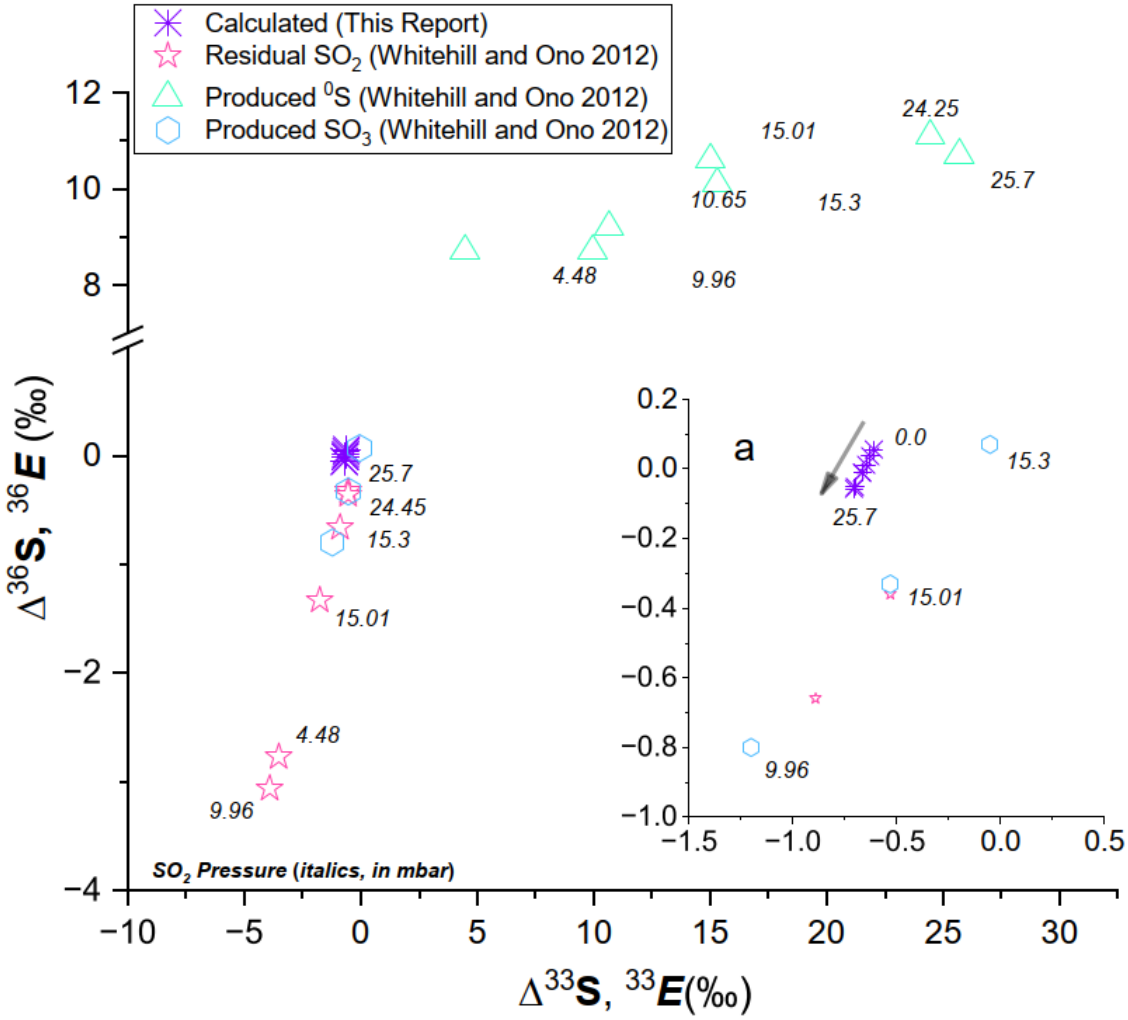

Figure 15: Calculated ^{33}E vs. ^{36}E isotopic effects from spectra reported in this study using a 150W Xenon arc lamp spectrum and compared to experiments by Whitehill et al. (2013)) ($\Delta^{33}S$ and $\Delta^{36}S$).

3.4 Geochemical implications

The origin of S-MIF found in stratospheric sulfate aerosols (SSA) is still debated. Savarino et al. (2003) attributed the S-MIF to SO_2 photoexcitation, because the SSA array of $\Delta^{36}S/\Delta^{33}S \approx -4.3$ matched early photoexcitation experimental results where KrF excimer laser (248 nm of narrow band) was used ($\Delta^{36}S$ vs $\Delta^{33}S$ slope ≈ -4.2; Farquhar et al., 2001). It is suspected that experiments using narrow-band UV spectra, which are significantly different from the sunlight spectrum, do not simulate isotope fractionation in the atmosphere (e.g., Claire et al., 2014). Subsequently, Danielache et al. (2012) reported $^{32,33,34,36}SO_2$ absorption cross-section

measurements for the $\tilde{B}^1B_1$-$\tilde{X}^1A_1$ band, allowing predictions of sulfur isotopic compositions in sulfate aerosols under various atmospheric conditions. Then, Hattori et al. (2013) modeled chemical reaction networks with a one-box model and calculated the isotope ratio of sulfate, assuming that SO_2 photoexcitation causes MIF with the $^{32,33,34,36}SO_2$ absorption cross-section measurements. The results of $\Delta^{33}S$ magnitudes and $\Delta^{36}S/\Delta^{33}S$ ratios in sulfates reproduce those within the SSA array. Thus, it is suggested that SO_2 photoexcitation (reaction R1) is the origin of the S-MIF in SSA. However, this result strongly depends on the results of the absorption cross-section measurements by Danielache et al. (2012). In this section we compare photoexcitation induced enrichment factors calculated from reported cross-sections to ice core data reported by Gautier et al. (2018), Shaheen et al. (2013) and Baroni et al. (2008). Gautier et al. (2018) have updated $\Delta^{36}S/\Delta^{33}S$ ratio to -1.56 ± 0.25 for records of the past 2,600 years, further modeling is required to explain the discrepancies between models based on spectra and observations. However, the $\Delta^{36}S/\Delta^{33}S$'s difference of the updated data by Gautier et al. (2018) may not be significant to determine the origin of S-MIF. The $\Delta^{36}S/\Delta^{33}S$ slope can be changed by mixing processes between mass-independent and mass-dependent sulfur species, that is, when non-zero $\Delta^{33}S$ signature is "diluted." This process happens because of the non-linearity character of the $\Delta^{33}S$ and $\Delta^{36}S$ definitions (Endo et al. under review).

Attenuation by atmospheric shielding of UV light below 300 nm renders all possible photoexcitations unlikely below 10 km. At an altitude of 30 km, the band of available UV radiation expands to 290 nm, and at an altitude of 40 km, UV light with wavelength longer than 280 nm can participate in the reaction. At 50 km of altitude, the atmospheric shielding effect significantly weakens, and the entire SO_2 UV absorption $\tilde{B}^1B_1$-$\tilde{X}^1A_1$ band contributes to the photoexcitation process (See **Figure S7**). Solar flux at different altitudes generates different S-MIF signatures on the SO_2 photoexcitation reaction. Solar flux at different altitudes used in the calculation of altitude dependent photoexcitation rate constants were obtained from modelled current atmosphere (Danielache et al., 2023) using actinic solar flux (Gueymard, 2004) at the top of atmosphere. The results of isotopic fractionation of self-shielding free SO_2 photoexcitation reaction (250−320 nm) are shown in **Figure 16** (brown circles).

The same calculation at different altitudes combined with self-shielding under an SO_2 column density ranging from 1.21×10^{14} to 1.21×10^{16} molecules cm^{-2} are shown in **Figure 16** (violet and yellow tringles), and for SO_2 column densities up to 1.21×10^{17} molecules cm^{-2} which are closer to those reported during the Pinatubo eruption are presented in **Figure 17**. For a further comparison, comparisons isotopic effects calculated by Hattori et al. (2013) are added to **Figure 17**. **Figure 16** also shows volcanic data from Gautier et al. (2018) (red stars), Shaheen et al., (2014) (black stars) and Baroni et al., (2008) (violet stars). Self-shielding free photoexcitation effect is almost 0 in ^{33}E and stays unchanged with altitude, ^{36}E range from −10‰ at 10 km to 4‰ at 30 km. Altitude variability do not produce any significant $^{36}E/^{33}E$ slope but it they show an interesting overlap with volcanic data suggesting that the ^{36}E variability is produced by altitude. Self-shielding calculations show a more revealing result in which increased column density (up to 1.21×10^{16} molecules cm^{-2}) creates a $^{36}E/^{33}E$ slope compatible with the reported volcanic data. The data presented in **Figure 17** includes the data in **Figure 16** but it has expanded both ^{33}E and ^{36}E axis. By expanding the ^{33}E and ^{36}E axis, self-shielding calculations more realistic to a stratospheric eruption (1.21×10^{17} molecules cm^{-2}) shows that the slope does not change but also is compatible and of reverse signs to the altitude and self-shielding

656 calculations of Hattori et al. (2013) and also $^{36}E/^{33}E$ slope compatible with volcanic reported
657 data.

658

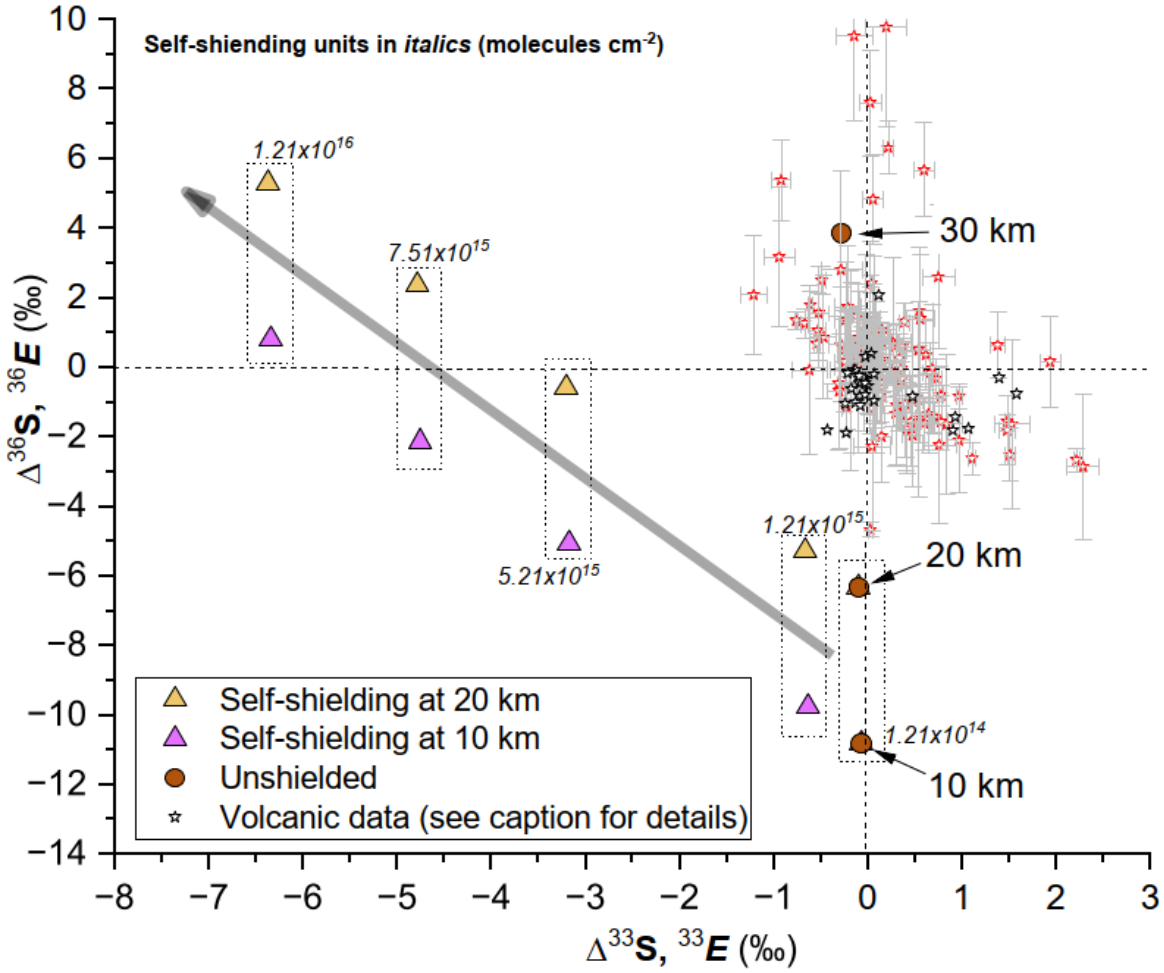

659

660 **Figure 16**: The isotopic fractionation from SO_2 photoexcitation using modern atmospheric
661 solar flux at different altitudes and comparison with Hattori et al. (2013). (a) $^{34}\varepsilon$ and ^{33}E. (b)
662 ^{33}E and ^{36}E. The volcanic data is from Gautier et al. (2018) (red stars), Shaheen et al. (2013)
663 (black stars) and Baroni et al. (2008) (violet stars).

664

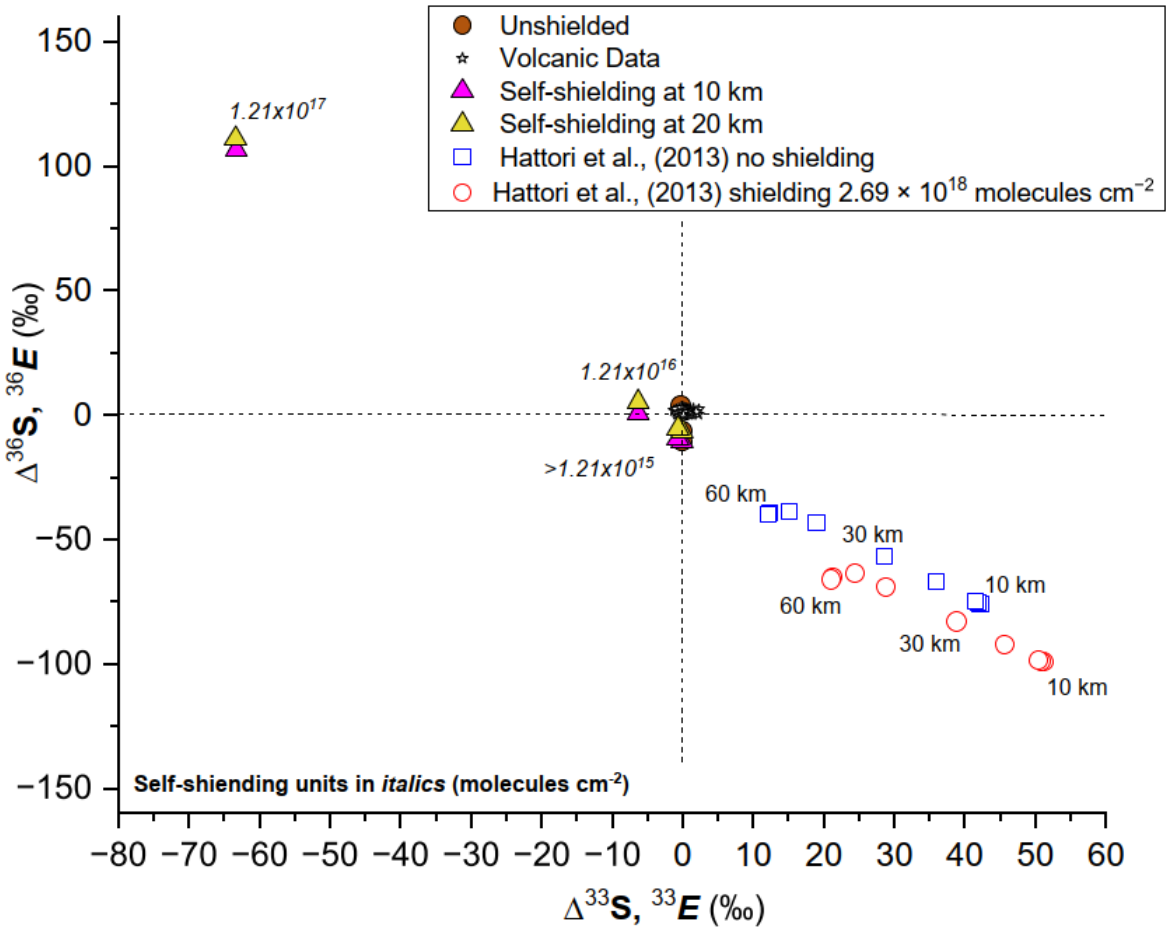

Figure 17: Photoexcitation enrichment factors calculated from this report compared to those reported by Hattori et al. (2013). Self-shielding calculation with column densities of 10^{19} molecules cm^{-2} (530 DU) as suggested by Guo et al. (2004) produced values of ^{36}E = 1.314‰ and ^{33}E = 1.163‰ which fall well outside of the range in the plot.

4 Conclusions

This study presents the cross-sections of $^{32}SO_2$, $^{33}SO_2$, $^{34}SO_2$, and $^{36}SO_2$ for the $\tilde{B}^1B_1$-$\tilde{X}^1A_1$ absorption band at 293.15 K measured at a resolution of 0.4 cm^{-1} with an error of 3−10%. In this report we implemented an algorithm using the LAD linear regression which was applied to finely calibrate the linear relationship between absorbance and pressure and then achieve the cross-section data at each wavelength. The overall features of measured cross-sections, that is, the peak positions of isotopologues, are consistent with previous studies (Danielache et al., 2008; Danielache et al., 2012). We obtained both more detail in the absorption peaks and a significant improvement in errors derived from noise during the measurement. For S-MIF related to SO_2 photochemistry, S-MIF predicted from our new spectral measurements do not reproduce results of S-MIF observed in SO_2 photochemical experiments performed by Whitehill et al. (2013). The discrepancy supports Whitehill's argument that large S-MIF originates in the intersystem crossing rather than photoexcitation alone.

685

Acknowledgements

686 **Acknowledgements**

687 This study does not have real or perceived financial conflict of interest for any author. We
688 would like to thank Shohei Hattori and Naohiro Yoshida for sample preparation and Matthew
689 S. Johnson for technical advice. We also wish to thank Yi Ding for his consultation and advice
690 on machine learning and algorithms. This research was funded by JSPS KAKENHI (grant
691 numbers 22H05150 and 20H01975).

Data Availability Statement

692 **Data Availability Statement**

693 The spectral data presented in this manuscript was recorded at the Tokyo Institute of
694 Technologies with experimental devices described in the experimental section. Reported data
695 set in this study are available at Harvard Dataverse repository of research data via
696 https://doi.org/10.7910/DVN/AP8ISE with CC0 1.0 license/Data use agreement. Figures were
697 made with Origin Ver. 2022 (Origin Lab). The code used in this manuscript for the calculation
698 of absorption cross-sections is licensed under MIT and Published on GitHub
699 https://github.com/PatrickYLi/LAD-Regression/tree/multi-core and Zenodo
700 (doi/10.5281/zenodo.10836723)
701

References

702 **References**

703 Anderson, R. J., and P. R. Griffiths (1975), Errors in absorbance measurements in infrared Fourier
704 transform spectrometry because of limited instrument resolution, *Analytical Chemistry*, *47*(14), 2339-
705 2347, doi:10.1021/ac60364a030.
706 Baroni, M., J. Savarino, J. Cole-Dai, V. K. Rai, and M. H. Thiemens (2008), Anomalous sulfur
707 isotope compositions of volcanic sulfate over the last millennium in Antarctic ice cores, *J. Geophys.*
708 *Res. Atmos.*, *113*(D20).
709 Baroni, M., M. H. Thiemens, R. J. Delmas, and J. Savarino (2007), Mass-independent sulfur isotopic
710 compositions in stratospheric volcanic eruptions, *Science*, *315*(5808), 84-87,
711 doi:10.1126/science.1131754.
712 Barra, I., L. Khiari, S. M. Haefele, R. Sakrabani, and F. Kebede (2021), Optimizing setup of scan
713 number in FTIR spectroscopy using the moment distance index and PLS regression: application to
714 soil spectroscopy, *Scientific reports*, *11*(1), 1-9, doi:10.1038/s41598-021-92858-w.
715 Blackie, D., R. Blackwell-Whitehead, G. Stark, J. C. Pickering, P. L. Smith, J. Rufus, and A. P.
716 Thorne (2011), High-resolution photoabsorption cross-section measurements of SO_2 at 198 K from
717 213 to 325 nm, *J. Geophys. Res.*, *116*(E3), doi:10.1029/2010je003707.
718 Claire, M. W., J. F. Kasting, S. D. Domagal-Goldman, E. E. Stüeken, R. Buick, and V. S. Meadows
719 (2014), Modeling the signature of sulfur mass-independent fractionation produced in the Archean
720 atmosphere, *Geochimica et Cosmochimica Acta*, *141*, 365-380, doi:10.1016/j.gca.2014.06.032.
721 Danielache, S. O., C. Eskebjerg, M. S. Johnson, Y. Ueno, and N. Yoshida (2008), High-precision
722 spectroscopy of ^{32}S, ^{33}S, and ^{34}S sulfur dioxide: Ultraviolet absorption cross sections and isotope
723 effects, *J. Geophys. Res. Atmos.*, *113*(D17), doi:10.1029/2007JD009695.

Danielache, S. O., S. Hattori, M. S. Johnson, Y. Ueno, S. Nanbu, and N. Yoshida (2012), Photoabsorption cross-section measurements of ^{32}S, ^{33}S, ^{34}S, and ^{36}S sulfur dioxide for the B^1B_1-X^1A_1 absorption band, *J. Geophys. Res. Atmos.*, *117*(D24), doi:10.1029/2012jd017464.

Danielache, S. O., G. Iwama, M. Shinkai, M. Oinuma, E. Simoncini, and T. Grassi (2023), Introducing atmospheric photochemical isotopic processes to the PATMO atmospheric code, *Geochem. J.*, *57*(2), 42-58, doi:10.2343/geochemj.GJ23004.

Dreissig, I., S. Machill, R. Salzer, and C. Krafft (2009), Quantification of brain lipids by FTIR spectroscopy and partial least squares regression, *Spectrochimica Acta Part A: Molecular and Biomolecular Spectroscopy*, *71*(5), 2069-2075, doi:10.1016/j.saa.2008.08.008.

Eiler, J. M., B. Bergquist, I. Bourg, P. Cartigny, J. Farquhar, A. Gagnon, W. Guo, I. Halevy, A. Hofmann, and T. E. Larson (2014), Frontiers of stable isotope geoscience, *Chem. Geol.*, *372*, 119-143, doi:10.1016/j.chemgeo.2014.02.006.

Endo, Y., S. O. Danielache, and Y. Ueno (2019), Total pressure dependence of sulfur mass-independent fractionation by SO_2 photolysis, *Geophys Res Lett*, *46*(1), 483-491, doi:10.1029/2018gl080730.

Endo, Y., S. O. Danielache, Y. Ueno, S. Hattori, M. S. Johnson, N. Yoshida, and H. G. Kjaergaard (2015), Photoabsorption cross-section measurements of ^{32}S, ^{33}S, ^{34}S, and ^{36}S sulfur dioxide from 190 to 220 nm, *Journal of Geophysical Research: Atmospheres*, *120*(6), 2546-2557, doi:10.1002/2014JD021671.

Endo, Y., S. O. Danielache, M. Ogawa, and Y. Ueno (2022a), Absorption spectra measurements at ~1 cm^{-1} spectral resolution of ^{32}S, ^{33}S, ^{34}S, and ^{36}S sulfur dioxide for the 206–220 nm region and applications to modeling of the isotopic self-shielding, *Geochemical Journal*, *56*(1), 40-56, doi:10.2343/geochemj.GJ22004.

Endo, Y., Sekine, Y., and Ueno, Y. (2022b). Sulfur mass-independent fractionation during SO_2 photolysis in low-temperature/pressure atmospheres. *Chemical Geology*, 609, 121064. doi.org/10.1016/j.chemgeo.2022.121064

Endo, Y., Y. Ueno, S. Aoyama, and S. O. Danielache (2016), Sulfur isotope fractionation by broadband UV radiation to optically thin SO_2 under reducing atmosphere, *Earth and Planetary Science Letters*, *453*, 9-22, doi:10.1016/j.epsl.2016.07.057.

Farquhar, J., H. Bao, and M. Thiemens (2000), Atmospheric influence of Earth's earliest sulfur cycle, *Science*, *289*(5480), 756-758, doi:science.289.5480.756.

Farquhar, J., J. Savarino, S. Airieau, and M. H. Thiemens (2001), Observation of wavelength-sensitive mass-independent sulfur isotope effects during SO_2 photolysis: Implications for the early atmosphere, *Journal of Geophysical Research: Planets*, *106*(E12), 32829-32839, doi:10.1029/2000JE001437.

Gautier, E., J. Savarino, J. Erbland, and J. Farquhar (2018), SO_2 oxidation kinetics leave a consistent isotopic imprint on volcanic ice core sulfate, *J. Geophys. Res. Atmos.*, *123*(17), 9801-9812.

Gueymard, C. A. (2004), The sun's total and spectral irradiance for solar energy applications and solar radiation models, *Solar energy*, *76*(4), 423-453, doi:10.1016/j.solener.2003.08.039.

Guo, S., Bluth, G. J. S., Rose, W. I., Watson, I. M., & Prata, A. J. (2004). Re-evaluation of SO_2 release of the 15 June 1991 Pinatubo eruption using ultraviolet and infrared satellite sensors. *Geochemistry, Geophysics, Geosystems*, *5*(4). https://doi.org/10.1029/2003GC000654

Hattori, S., J. A. Schmidt, M. S. Johnson, S. O. Danielache, A. Yamada, Y. Ueno, and N. Yoshida (2013), SO_2 photoexcitation mechanism links mass-independent sulfur isotopic fractionation in cryospheric sulfate to climate impacting volcanism, *Proceedings of the National Academy of Sciences*, *110*(44), 17656-17661, doi:10.1073/pnas.1213153110.

Heicklen, J., N. Kelly, and K. Partymiller (1980), The photophysics and photochemistry of SO2, *Reviews of Chemical Intermediates*, *3*(3-4), 315-404, doi:10.1007/bf03052425.

Herzberg, G. (1945), *Molecular spectra and molecular structure*, D. van Nostrand.

Hulston, J., and H. Thode (1965), Variations in the S^{33}, S^{34}, and S^{36} contents of meteorites and their relation to chemical and nuclear effects, *J. Geophys. Res.*, *70*(14), 3475-3484, doi:10.1029/JZ070i014p03475.

Koplow, J. P., D. A. Kliner, and L. Goldberg (1998), Development of a narrow-band, tunable, frequency-quadrupled diode laser for UV absorption spectroscopy, *Applied optics*, *37*(18), 3954-3960, doi:10.1364/AO.37.003954.

Kostkowski, H. J., and A. M. Bass (1956), Slit function effects in the direct measurement of absorption line half-widths and intensities, *JOSA*, *46*(12), 1060-1064, doi:10.1364/JOSA.46.001060.

Kroll, J. A., B. N. Frandsen, R. J. Rapf, H. G. Kjaergaard, and V. Vaida (2018), Reactivity of Electronically Excited SO_2 with Alkanes, *The Journal of Physical Chemistry A*, *122*(39), 7782-7789, doi:10.1021/acs.jpca.8b04643.

Kumar, P., J. Ellis, and B. Poirier (2015), Rovibrational bound states of SO_2 isotopologues. I: Total angular momentum J=0–10, *Chem. Phys.*, *450*, 59-73.

Leonard C. Entwicklung eines UV-laserspektroskopischen nachweisverfahrens für OH-Radikals und spektroskopische untersuchungen an spurengasen unter troposphärischen bedingungen, Germany: University of Hannover; 1989. Doctoral dissertation in physics.

Li, L., H. Zhao, N. Ni, Y. Wang, J. Gao, Q. Gao, Y. Zhang, and Y. Zhang (2022), Study on the origin of linear deviation with the Beer-Lambert law in absorption spectroscopy by measuring sulfur dioxide, *Spectrochimica Acta Part A: Molecular and Biomolecular Spectroscopy*, *275*, 121192, doi:10.1016/j.saa.2022.121192.

Lyons, J., H. Herde, G. Stark, D. Blackie, J. Pickering, and N. de Oliveira (2018), VUV pressure-broadening in sulfur dioxide, *Journal of Quantitative Spectroscopy and Radiative Transfer*, *210*, 156-164.

Masterson, A. L., J. Farquhar, and B. A. Wing (2011), Sulfur mass-independent fractionation patterns in the broadband UV photolysis of sulfur dioxide: Pressure and third body effects, *Earth and Planetary Science Letters*, *306*(3), 253-260, doi:10.1016/j.epsl.2011.04.004.

Mellqvist, J., and A. Rosén (1996), DOAS for flue gas monitoring—II. Deviations from the Beer-Lambert law for the UV/visible absorption spectra of NO, NO_2, SO_2 and NH_3, *Journal of Quantitative Spectroscopy and Radiative Transfer*, *56*(2), 209-224, doi:10.1016/0022-4073(96)00043-X.

Meyer-Jacob, C., H. Vogel, F. Boxberg, P. Rosén, M. E. Weber, and R. Bindler (2014), Independent measurement of biogenic silica in sediments by FTIR spectroscopy and PLS regression, *Journal of paleolimnology*, *52*, 245-255, doi:10.1007/s10933-014-9791-5.

Ono, S. (2017), Photochemistry of sulfur dioxide and the origin of mass-independent isotope fractionation in Earth's atmosphere, *Annual Review of Earth and Planetary Sciences*, *45*(1), 301-329, doi:10.1146/annurev-earth-060115-012324.

Origin, Version 2022. OriginLab Corporation, Northampton, MA, USA.

Pavlov, A., and J. Kasting (2002), Mass-independent fractionation of sulfur isotopes in Archean sediments: strong evidence for an anoxic Archean atmosphere, *Astrobiology*, *2*(1), 27-41, doi:10.1089/153110702753621321.

Pedregosa, F., G. Varoquaux, A. Gramfort, V. Michel, B. Thirion, O. Grisel, M. Blondel, P. Prettenhofer, R. Weiss, and V. Dubourg (2011), Scikit-learn: Machine learning in Python, *The Journal of machine Learning research*, *12*, 2825-2830.

Rufus, J., G. Stark, P. L. Smith, J. C. Pickering, and A. P. Thorne (2003), High-resolution photoabsorption cross section measurements of SO_2, 2: 220 to 325 nm at 295 K, *Journal of Geophysical Research: Planets*, *108*(E2), doi:10.1029/2002je001931.

Santos, V. H. J. M. D., D. Pontin, G. G. D. Ponzi, A. S. D. G. E. Stepanha, R. B. Martel, M. K. Schütz, S. M. O. Einloft, and F. Dalla Vecchia (2021), Application of Fourier Transform infrared spectroscopy (FTIR) coupled with multivariate regression for calcium carbonate (CaCO3) quantification in cement, *Construction and Building Materials*, *313*, 125413, doi:10.1016/j.conbuildmat.2021.125413.

Savarino, J., A. Romero, J. Cole-Dai, S. Bekki, and M. Thiemens (2003), UV induced mass-independent sulfur isotope fractionation in stratospheric volcanic sulfate, *Geophys. Res. Lett*, *30*(21), doi:10.1029/2003GL018134.

Shaheen, R., M. Abauanza, T. L. Jackson, J. McCabe, J. Savarino, and M. H. Thiemens (2013), Tales of volcanoes and El-Niño southern oscillations with the oxygen isotope anomaly of sulfate aerosol, *Proceedings of the National Academy of Sciences*, *110*(44), 17662-17667.

Skoog, D. A., F. J. Holler, and S. R. Crouch (2017), *Principles of instrumental analysis*, Cengage learning.

Stark, G., P. L. Smith, J. Rufus, A. Thorne, J. Pickering, and G. Cox (1999), High-resolution photoabsorption cross-section measurements of SO_2 at 295 K between 198 and 220 nm, *Journal of Geophysical Research: Planets*, *104*(E7), 16585-16590, doi:10.1029/1999JE001022.

Tsai, S.-M., E. K. Lee, D. Powell, P. Gao, X. Zhang, J. Moses, E. Hébrard, O. Venot, V. Parmentier, and S. Jordan (2023), Photochemically produced SO2 in the atmosphere of WASP-39b, *Nature*, *617*(7961), 483-487.

Ueno, Y., M. S. Johnson, S. O. Danielache, C. Eskebjerg, A. Pandey, and N. Yoshida (2009), Geological sulfur isotopes indicate elevated OCS in the Archean atmosphere, solving faint young sun paradox, *Proceedings of the National Academy of Sciences*, *106*(35), 14784-14789, doi:10.1073/pnas.0903518106.

Vandaele, A. C., C. Hermans, and S. Fally (2009), Fourier transform measurements of SO_2 absorption cross sections: II.: Temperature dependence in the 29 000–44 000 cm^{-1} (227–345 nm) region, *Journal of Quantitative Spectroscopy and Radiative Transfer*, *110*(18), 2115-2126, doi:10.1016/j.jqsrt.2009.05.006.

Whitehill, A., and S. Ono (2012), Excitation band dependence of sulfur isotope mass-independent fractionation during photochemistry of sulfur dioxide using broadband light sources, *Geochimica et Cosmochimica Acta*, *94*, 238-253, doi:10.1016/j.gca.2012.06.014.

Whitehill, A. R., C. Xie, X. Hu, D. Xie, H. Guo, and S. Ono (2013), Vibronic origin of sulfur mass-independent isotope effect in photoexcitation of SO_2 and the implications to the early earth's atmosphere, *Proceedings of the National Academy of Sciences*, *110*(44), 17697-17702, doi:10.1073/pnas.1306979110.

Wu, C. R., B. Yang, F. Chen, D. Judge, J. Caldwell, and L. Trafton (2000), Measurements of high-, room-, and low-temperature photoabsorption cross sections of SO_2 in the 2080- to 2950-Å region, with application to Io, *Icarus*, *145*(1), 289-296, doi:10.1006/icar.1999.6322.

Yung, Y. L., and W. B. DeMore (1999), *Photochemistry of planetary atmospheres*, Oxford University Press, USA, doi:10.1093/oso/9780195105018.001.0001.

Figure 1.

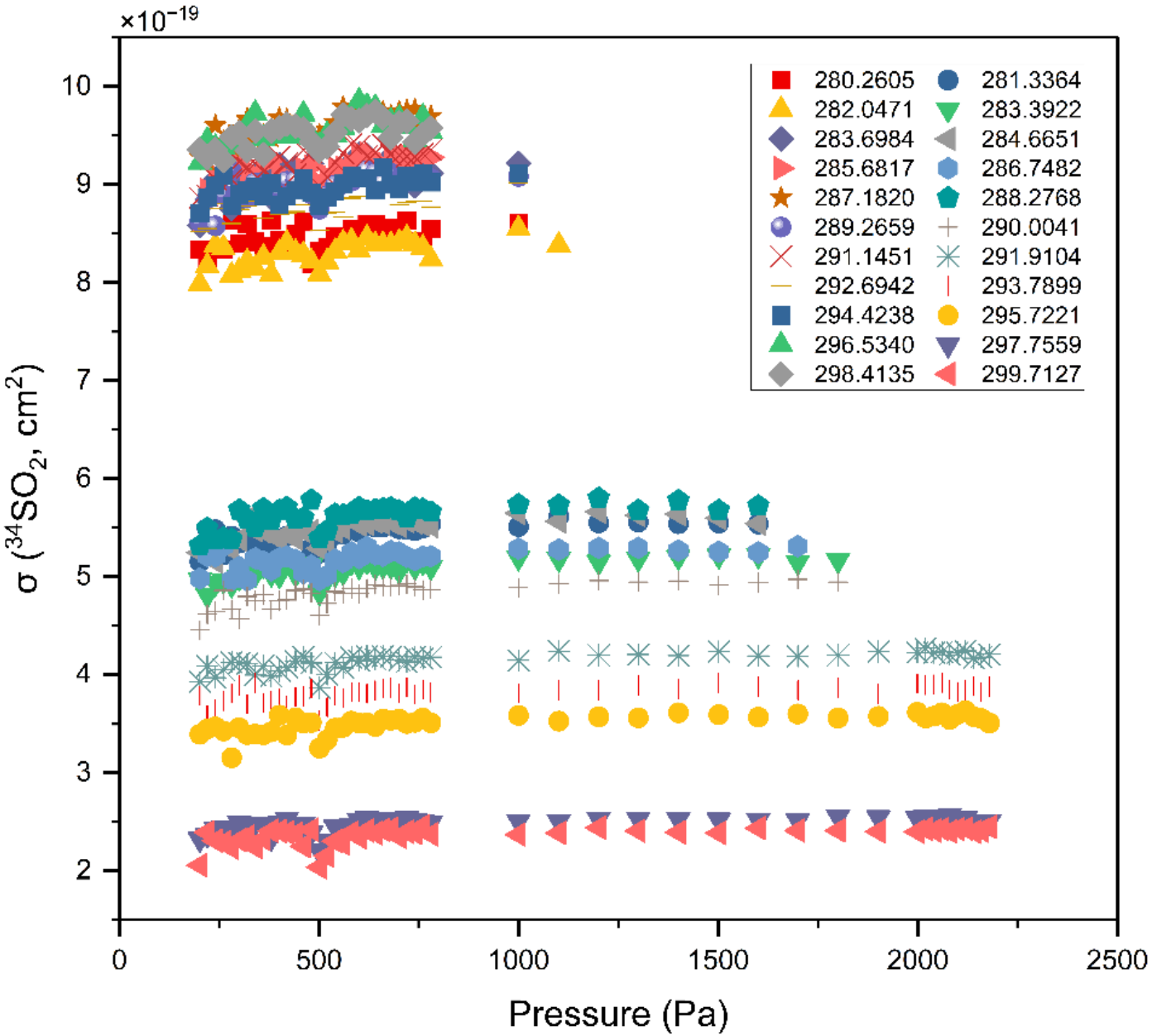
×10⁻¹⁹
σ (³⁴SO₂, cm²)
Pressure (Pa)
0
500
1000
1500
2000
2500
2
3
4
5
6
7
8
9
10
280.2605
281.3364
282.0471
283.3922
283.6984
284.6651
285.6817
286.7482
287.1820
288.2768
289.2659
290.0041
291.1451
291.9104
292.6942
293.7899
294.4238
295.7221
296.5340
297.7559
298.4135
299.7127

Figure 2.

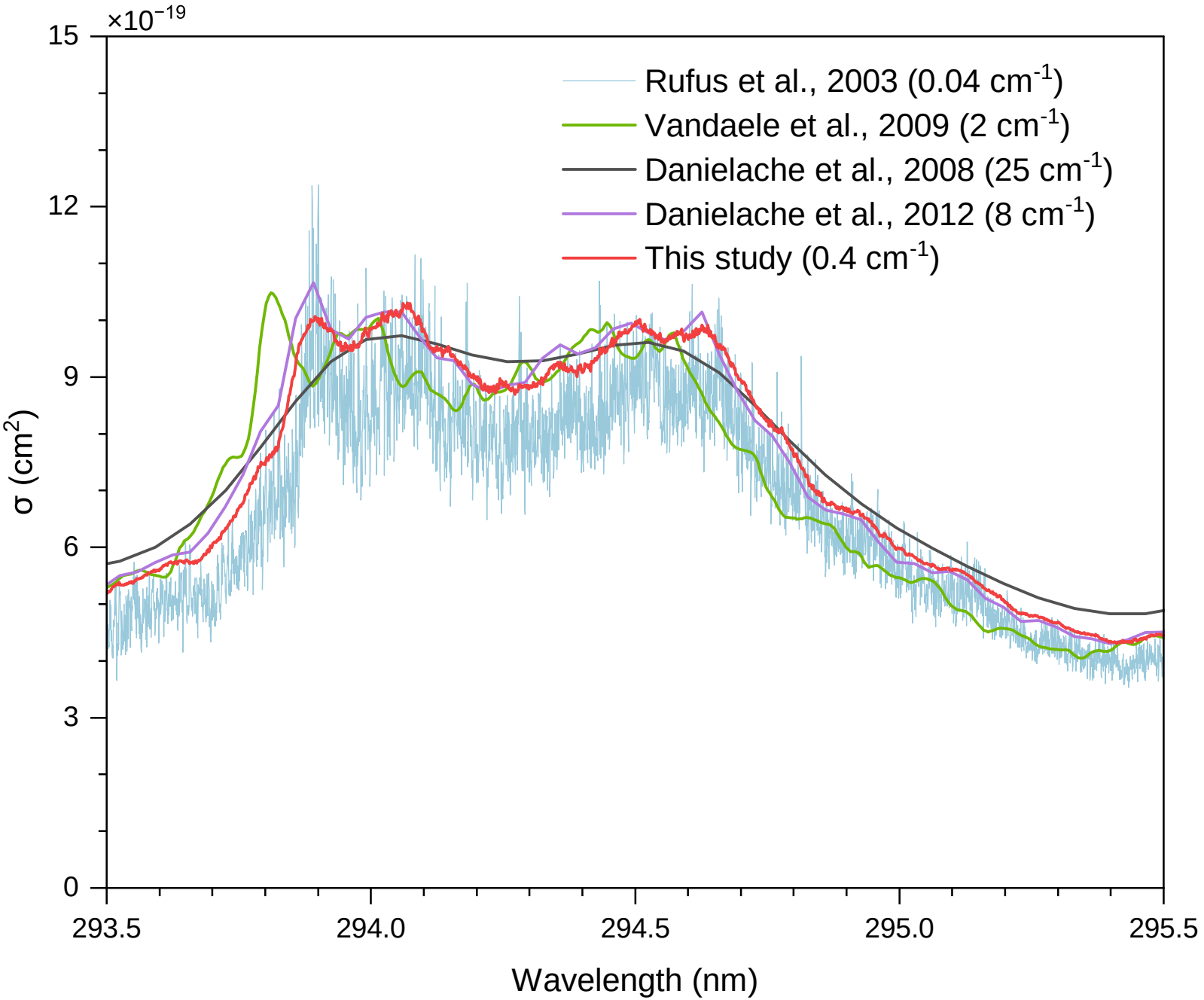
×10−19
15
12
9
6
3
0
σ (cm2)
293.5
294.0
294.5
295.0
295.5
Wavelength (nm)
Rufus et al., 2003 (0.04 cm-1)
Vandaele et al., 2009 (2 cm-1)
Danielache et al., 2008 (25 cm-1)
Danielache et al., 2012 (8 cm-1)
This study (0.4 cm-1)

Figure 3.

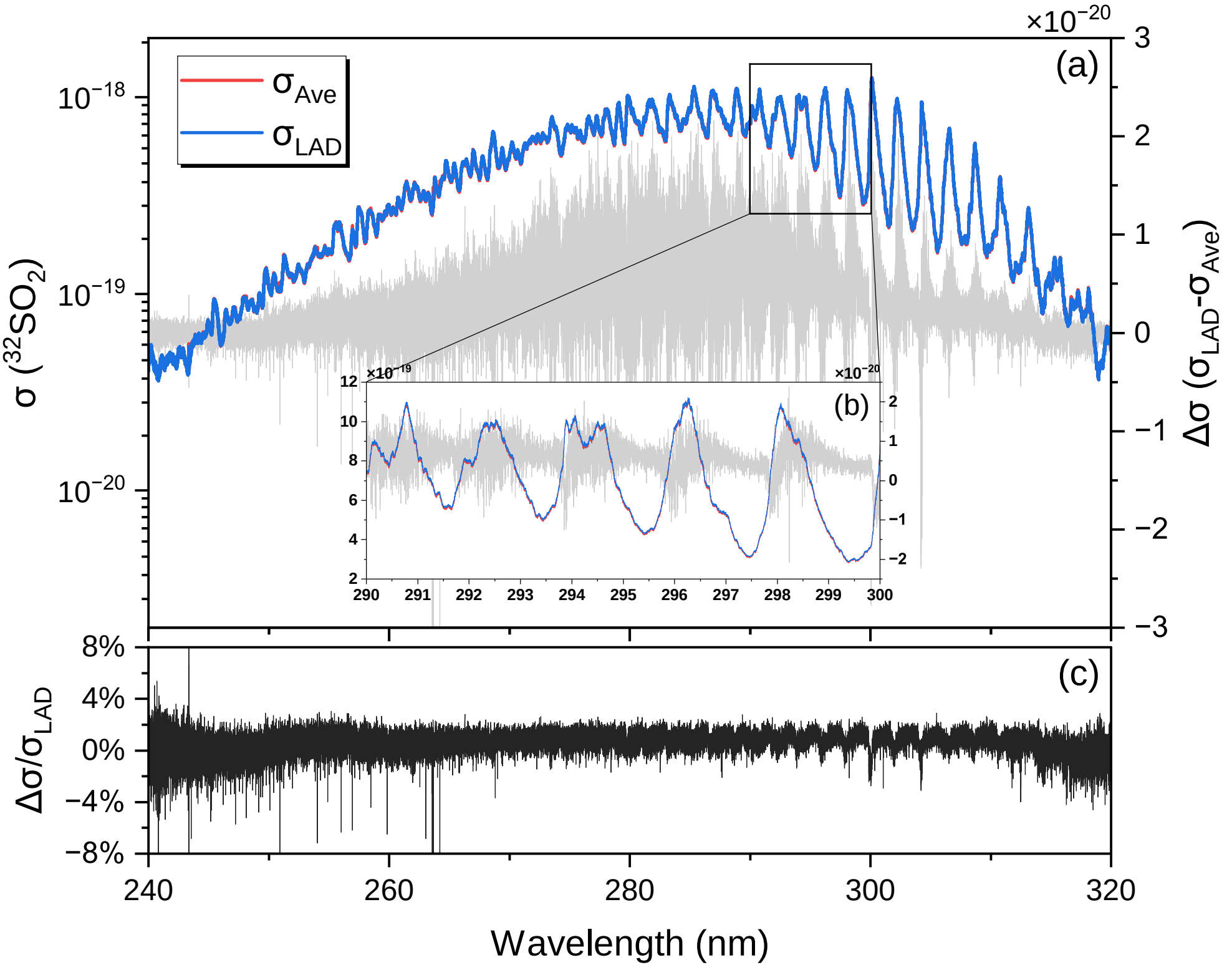
σ Ave
σ LAD
(a)
(b)
(c)
σ (32SO2)
Δσ (σLAD-σAve)
Δσ/σLAD
Wavelength (nm)
×10−20
×10−19
10−18
10−19
10−20
8%
4%
0%
−4%
−8%
240
260
280
300
320

Figure 4.

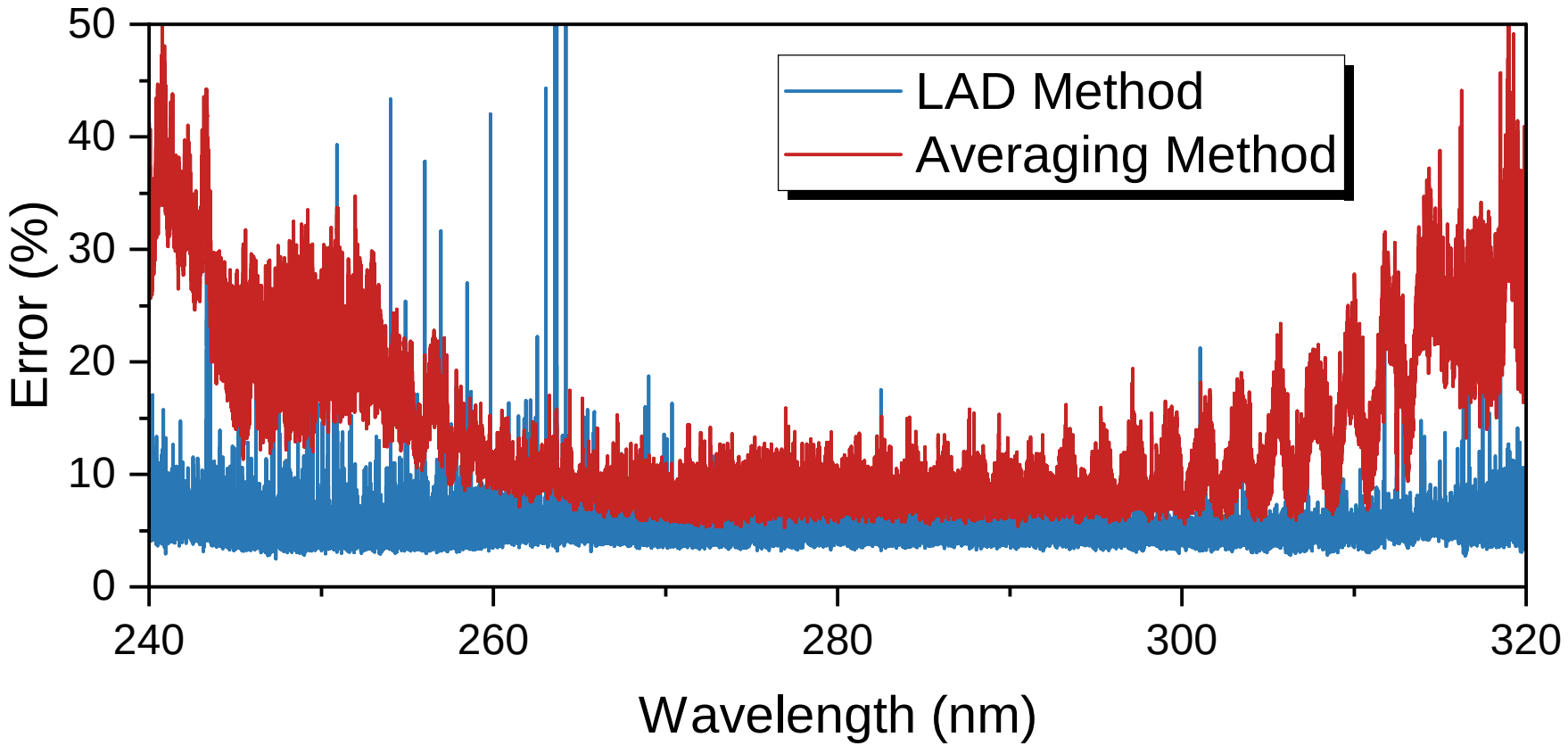
LAD Method
Averaging Method
Error (%)
Wavelength (nm)
0
10
20
30
40
50
240
260
280
300
320

Figure 5.

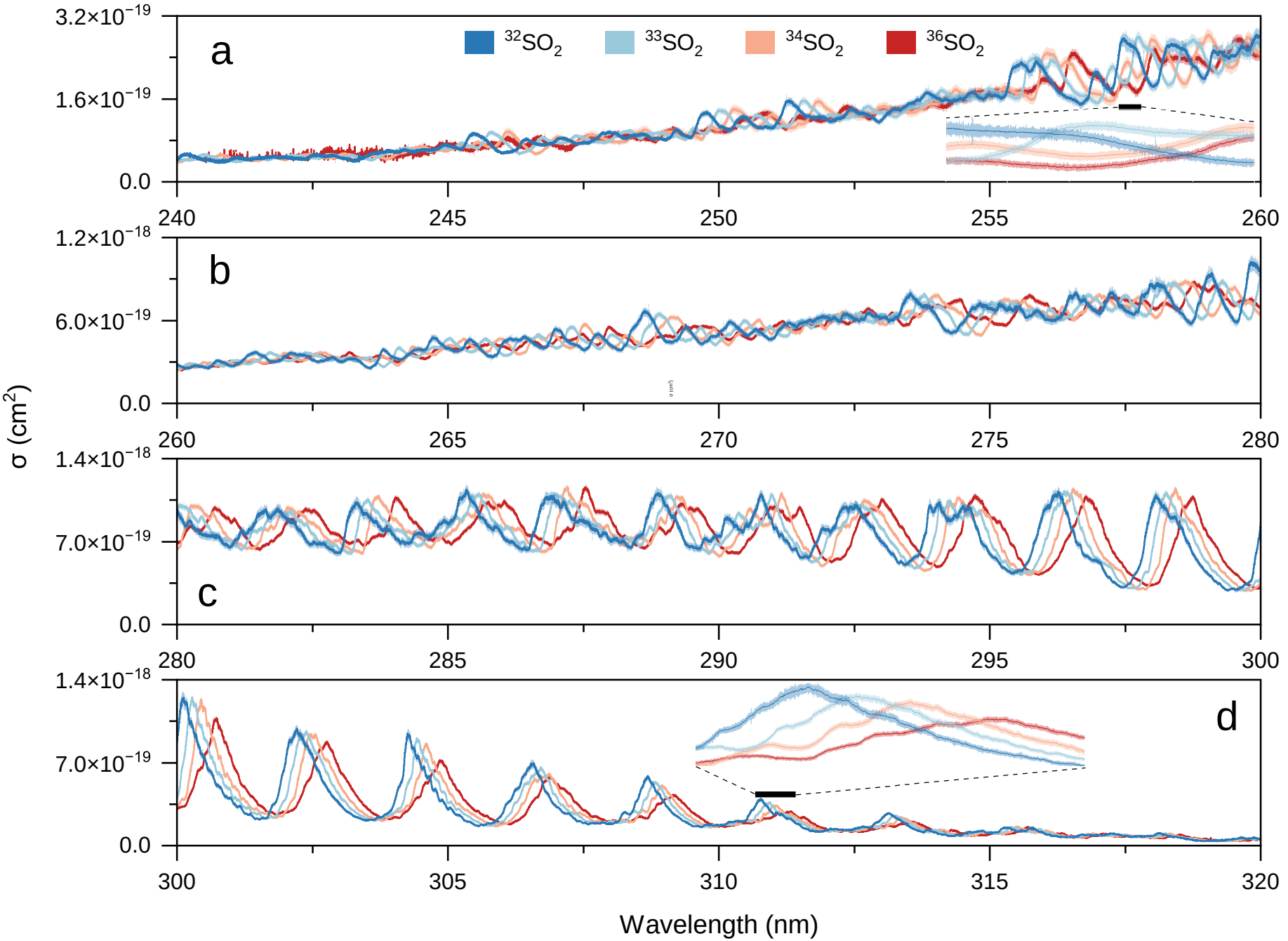
a
b
c
d
$^{32}SO_2$
$^{33}SO_2$
$^{34}SO_2$
$^{36}SO_2$
3.2×10⁻¹⁹
1.6×10⁻¹⁹
0.0
240
245
250
255
260
1.2×10⁻¹⁸
6.0×10⁻¹⁹
0.0
260
265
270
275
280
1.4×10⁻¹⁸
7.0×10⁻¹⁹
0.0
280
285
290
295
300
1.4×10⁻¹⁸
7.0×10⁻¹⁹
0.0
300
305
310
315
320
σ (cm²)
Wavelength (nm)

Figure 6.

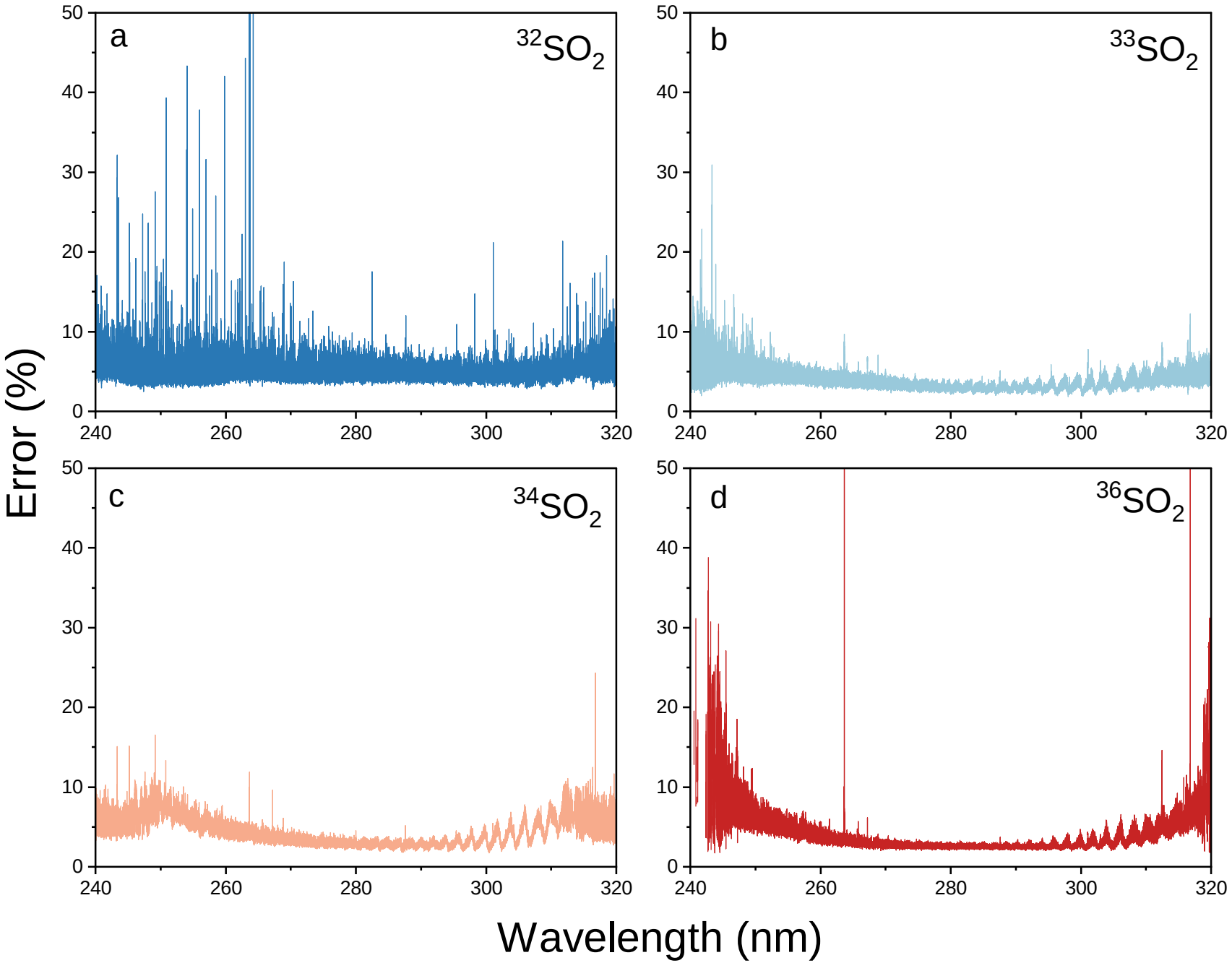
a
$^{32}SO_2$
b
$^{33}SO_2$
c
$^{34}SO_2$
d
$^{36}SO_2$
Error (%)
Wavelength (nm)
0
10
20
30
40
50
240
260
280
300
320

Figure 7.

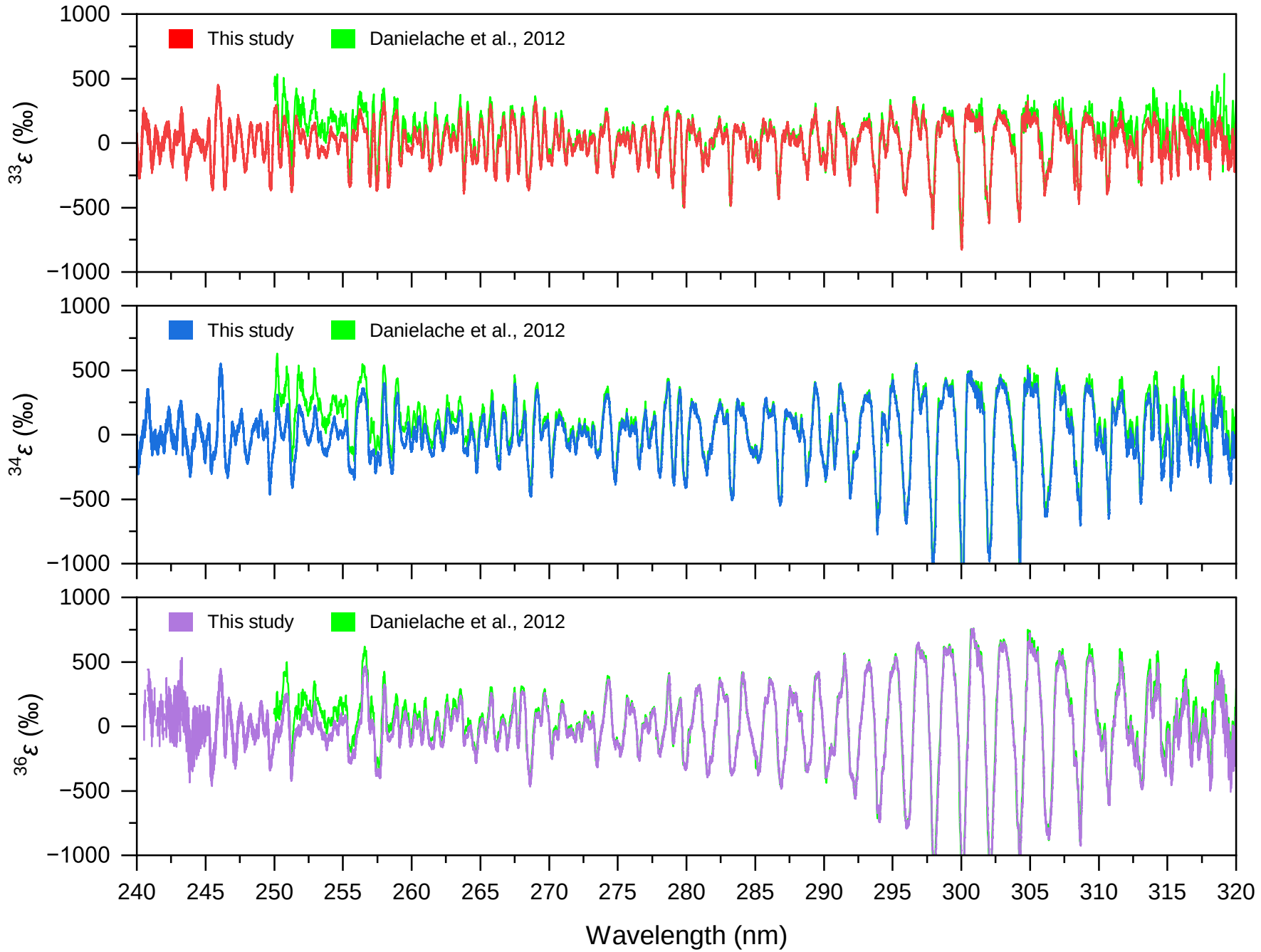
This study
Danielache et al., 2012
$^{33}\varepsilon$ (‰)
$^{34}\varepsilon$ (‰)
$^{36}\varepsilon$ (‰)
1000
500
0
−500
−1000
240
245
250
255
260
265
270
275
280
285
290
295
300
305
310
315
320
Wavelength (nm)

Figure 8.

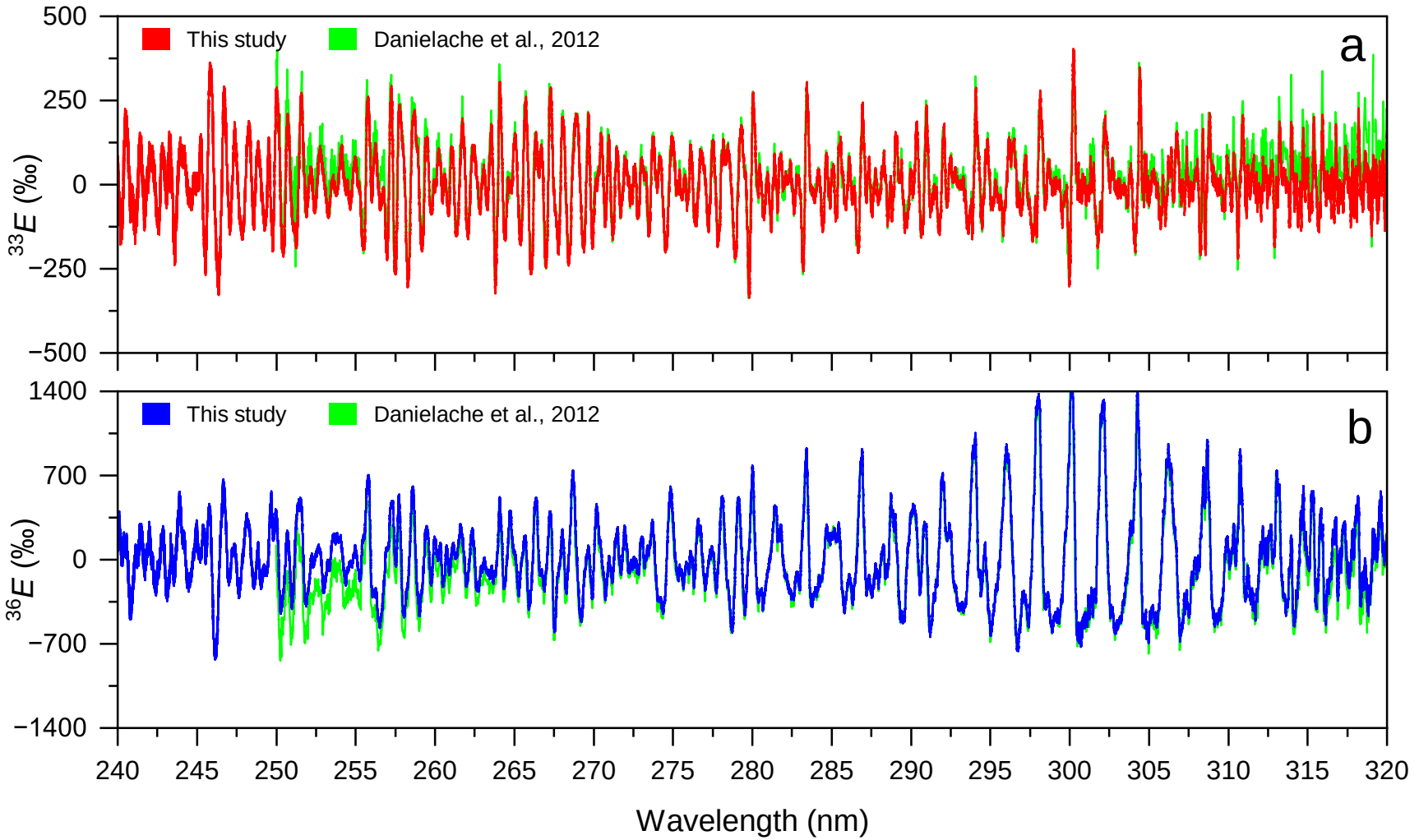
This study
Danielache et al., 2012
a
^{33}E (‰)
500
250
0
−250
−500
This study
Danielache et al., 2012
b
^{36}E (‰)
1400
700
0
−700
−1400
240
245
250
255
260
265
270
275
280
285
290
295
300
305
310
315
320
Wavelength (nm)

Figure 9.

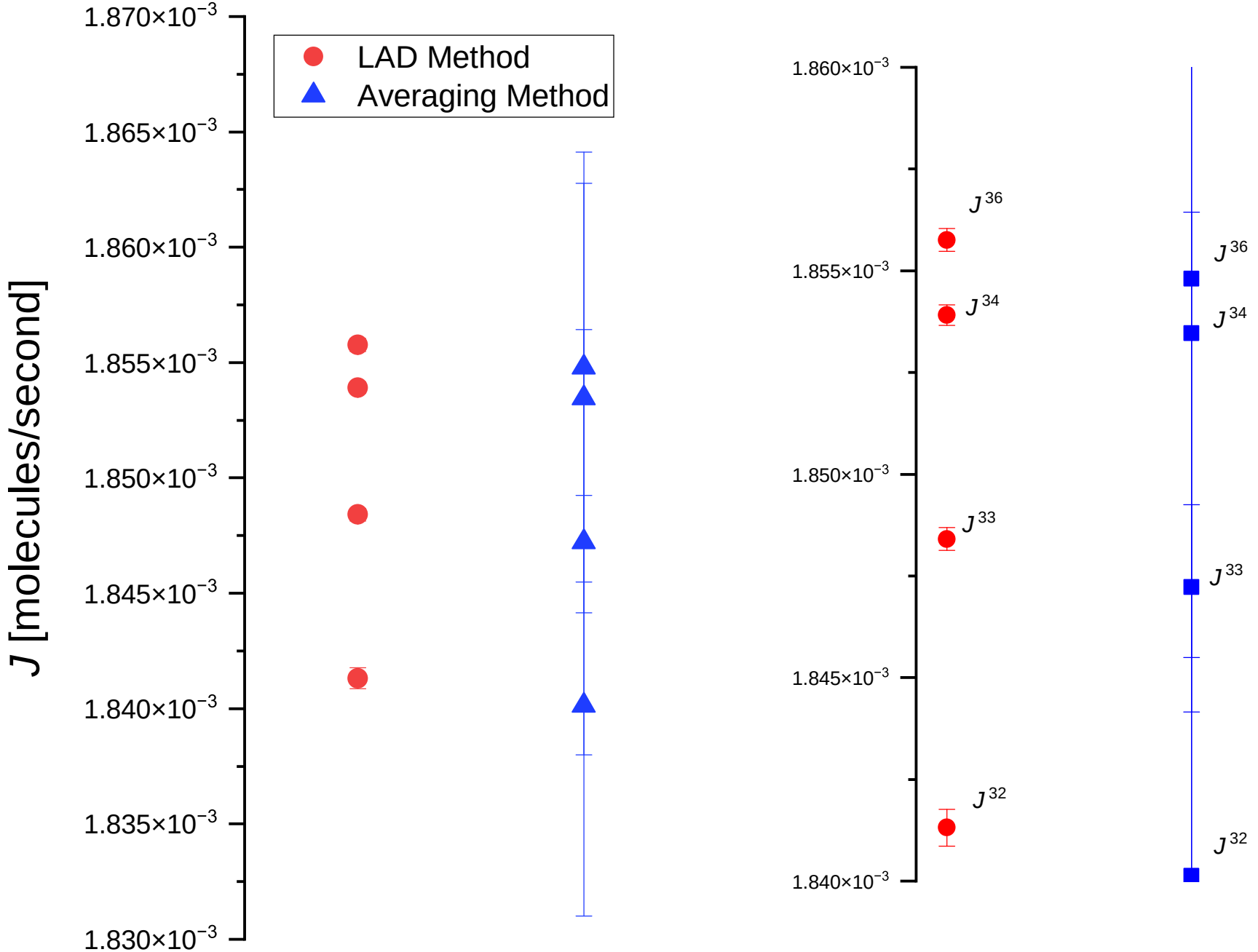
LAD Method
Averaging Method
J [molecules/second]
1.870×10−3
1.865×10−3
1.860×10−3
1.855×10−3
1.850×10−3
1.845×10−3
1.840×10−3
1.835×10−3
1.830×10−3
J 36
J 34
J 33
J 32

Figure 10.

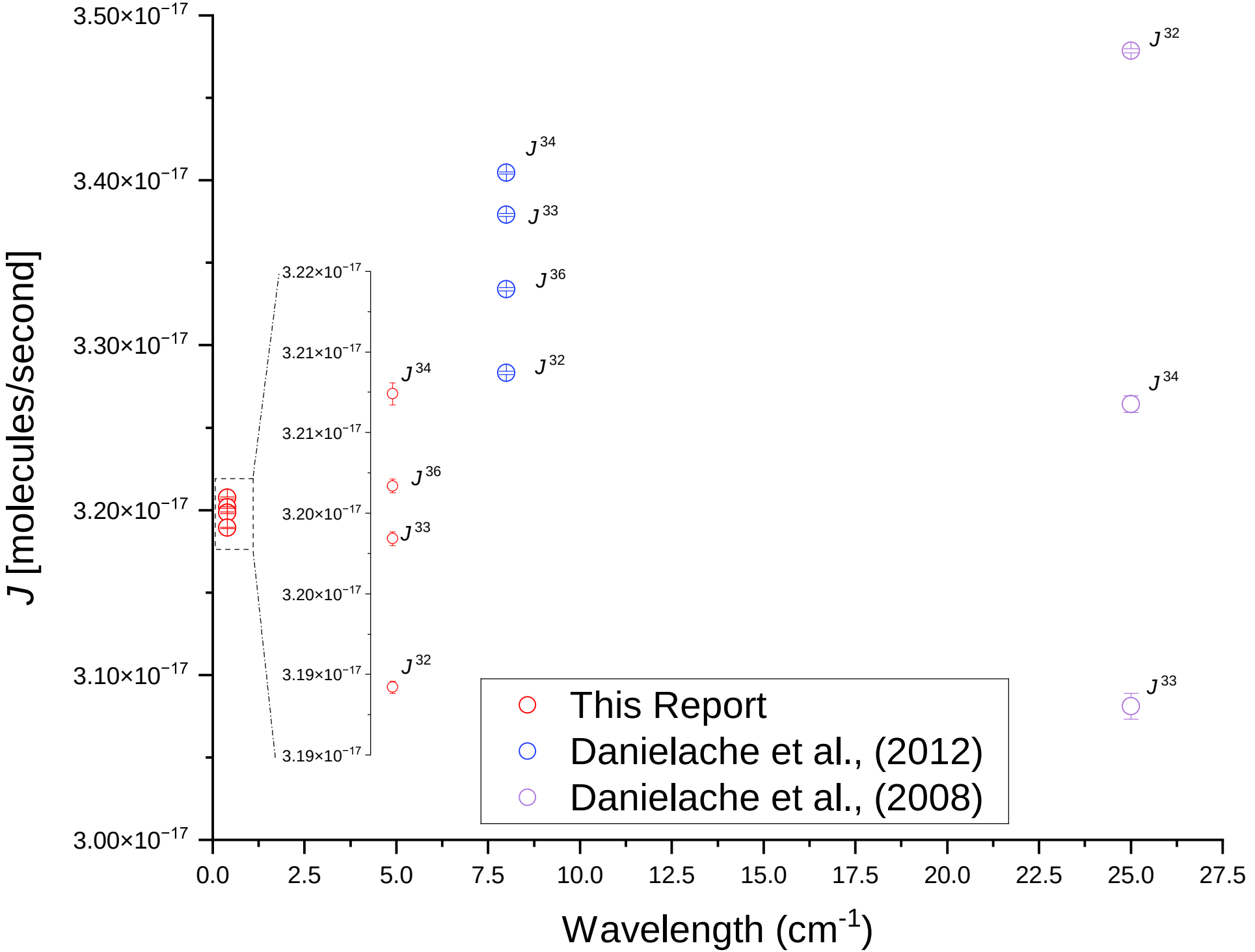
3.50×10−17
3.40×10−17
3.30×10−17
3.20×10−17
3.10×10−17
3.00×10−17
J [molecules/second]
0.0
2.5
5.0
7.5
10.0
12.5
15.0
17.5
20.0
22.5
25.0
27.5
Wavelength (cm-1)
J 32
J 34
J 33
J 36
J 32
J 34
J 33
3.22×10−17
3.21×10−17
3.21×10−17
3.20×10−17
3.20×10−17
3.19×10−17
3.19×10−17
J 34
J 36
J 33
J 32
This Report
Danielache et al., (2012)
Danielache et al., (2008)

Figure 11.

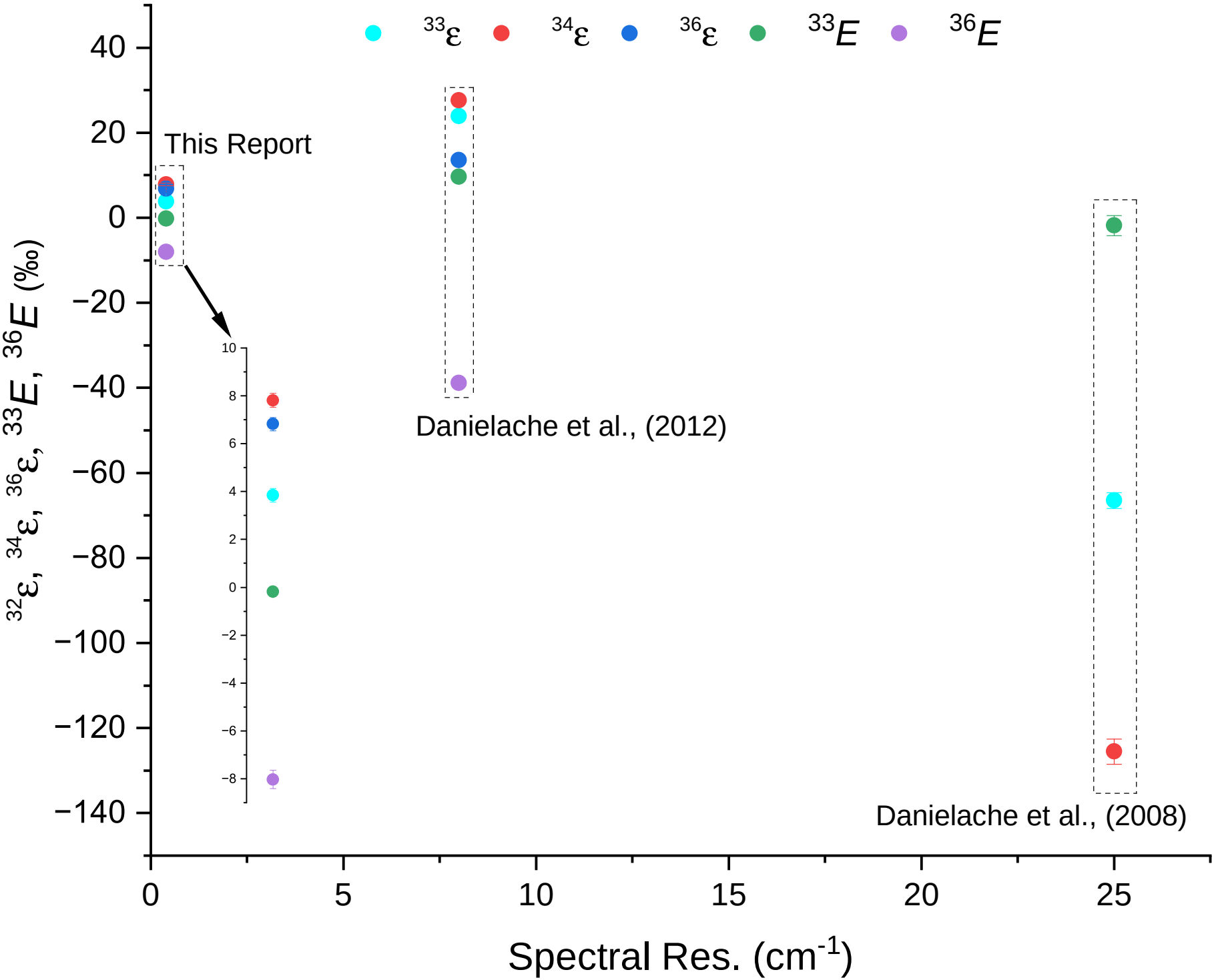
$^{33}\varepsilon$
$^{34}\varepsilon$
$^{36}\varepsilon$
^{33}E
^{36}E
This Report
Danielache et al., (2012)
Danielache et al., (2008)
$^{32}\varepsilon$, $^{34}\varepsilon$, $^{36}\varepsilon$, ^{33}E, ^{36}E (‰)
Spectral Res. (cm^{-1})
40
20
0
−20
−40
−60
−80
−100
−120
−140
0
5
10
15
20
25
10
8
6
4
2
0
−2
−4
−6
−8

Figure 12.

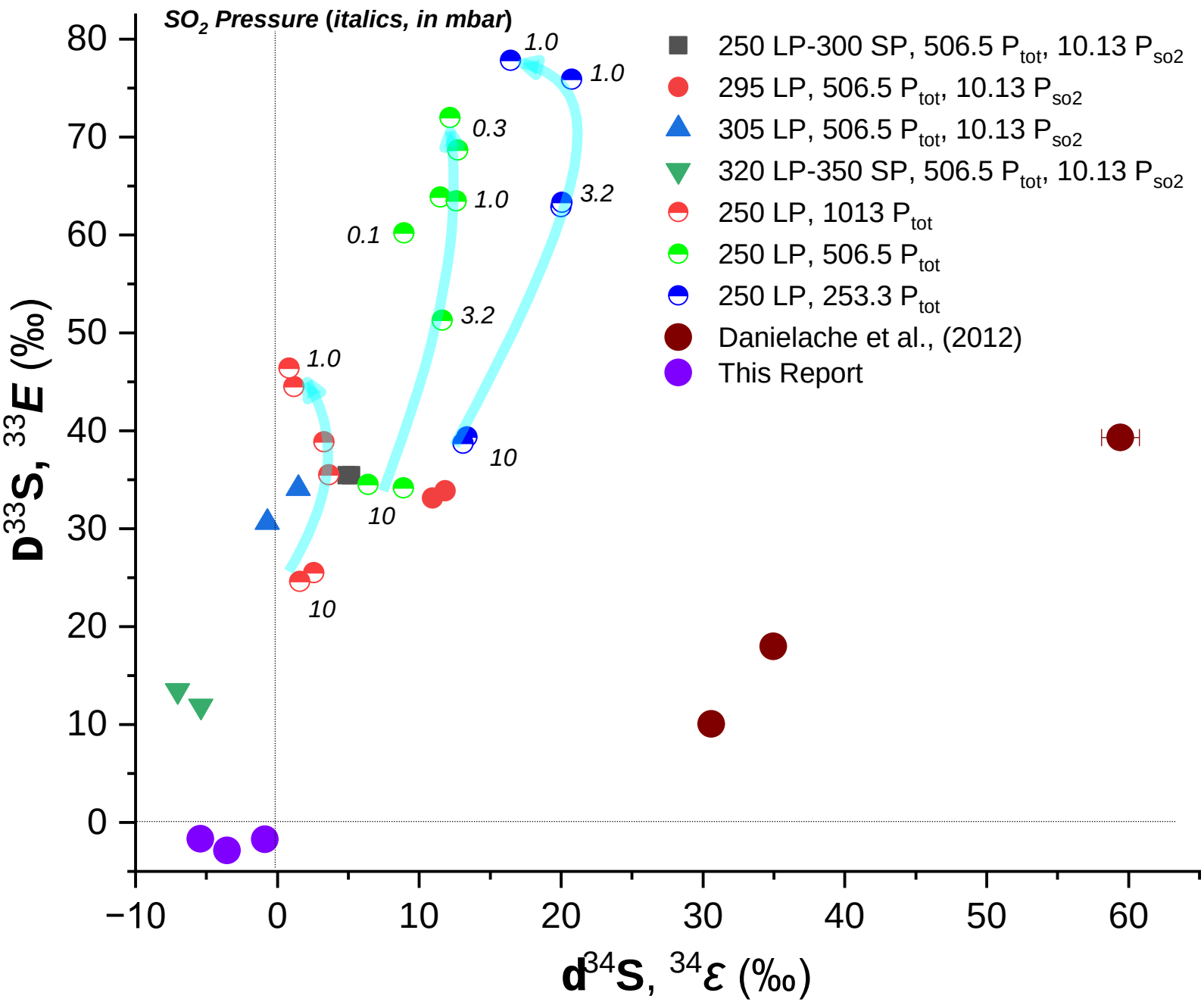
SO2 Pressure (italics, in mbar)
1.0
1.0
0.3
1.0
3.2
0.1
3.2
1.0
10
10
10
250 LP-300 SP, 506.5 Ptot, 10.13 Pso2
295 LP, 506.5 Ptot, 10.13 Pso2
305 LP, 506.5 Ptot, 10.13 Pso2
320 LP-350 SP, 506.5 Ptot, 10.13 Pso2
250 LP, 1013 Ptot
250 LP, 506.5 Ptot
250 LP, 253.3 Ptot
Danielache et al., (2012)
This Report
D33S, 33E (‰)
d34S, 34ε (‰)
80
70
60
50
40
30
20
10
0
−10
0
10
20
30
40
50
60

Figure 13.

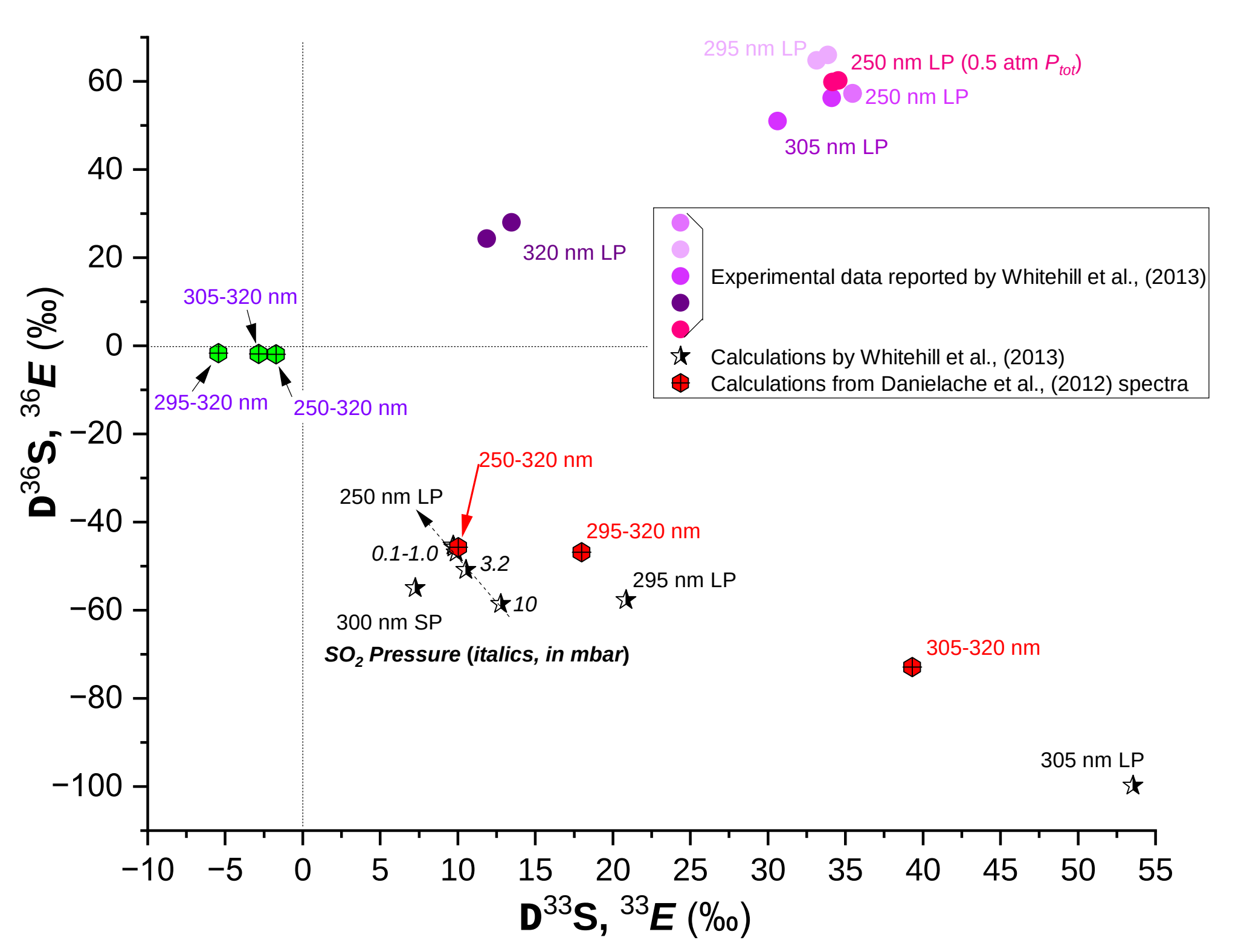
295 nm LP
250 nm LP (0.5 atm P_{tot})
250 nm LP
305 nm LP
320 nm LP
Experimental data reported by Whitehill et al., (2013)
Calculations by Whitehill et al., (2013)
Calculations from Danielache et al., (2012) spectra
305-320 nm
295-320 nm
250-320 nm
250-320 nm
250 nm LP
0.1-1.0
3.2
10
300 nm SP
295-320 nm
295 nm LP
305-320 nm
305 nm LP
SO2 Pressure (italics, in mbar)
D33S, 33E (‰)
D36S, 36E (‰)
60
40
20
0
−20
−40
−60
−80
−100
−10
−5
0
5
10
15
20
25
30
35
40
45
50
55

Figure 14.

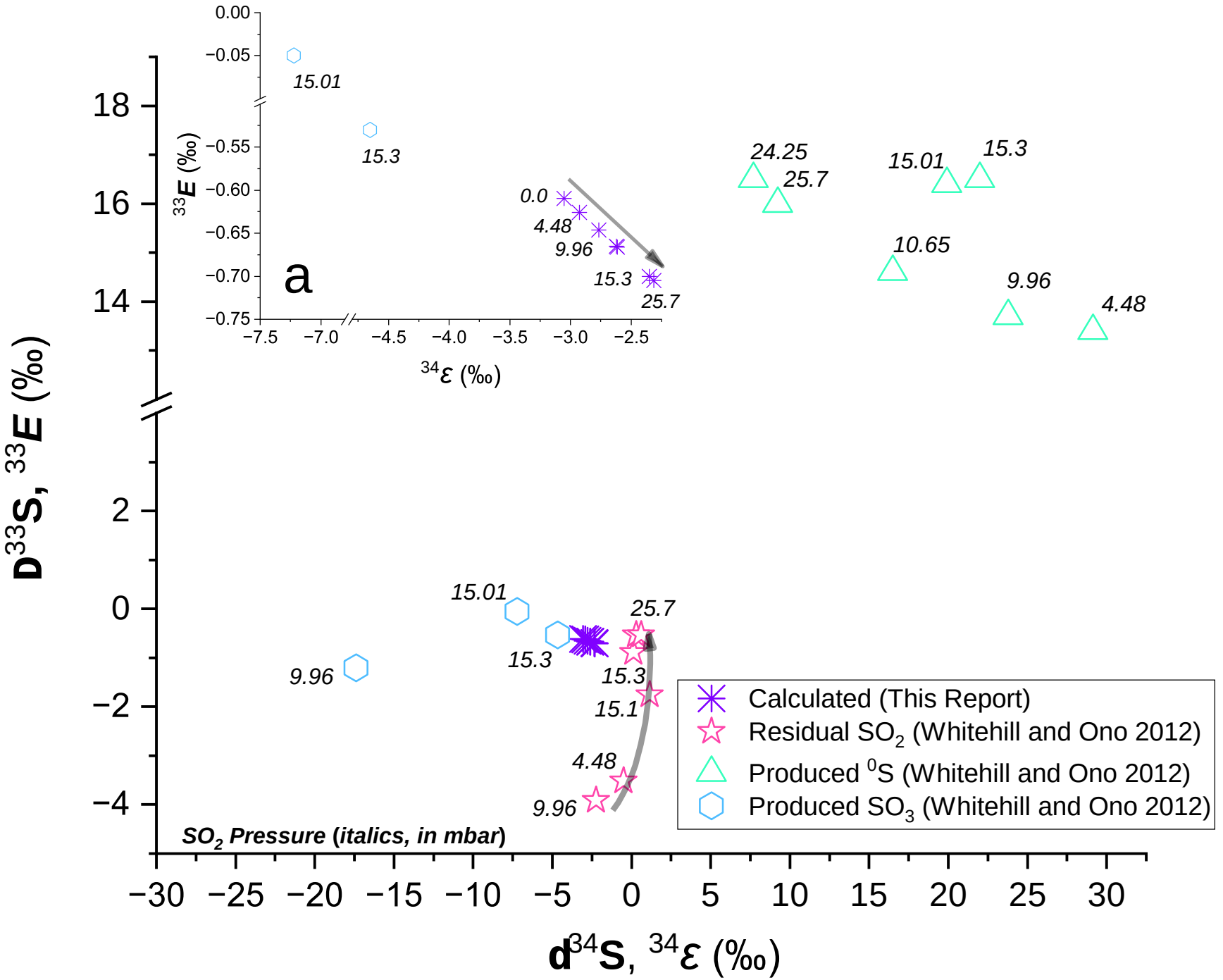
a
^{33}E (‰)
$^{34}\varepsilon$ (‰)
0.00
−0.05
−0.55
−0.60
−0.65
−0.70
−0.75
−7.5
−7.0
−4.5
−4.0
−3.5
−3.0
−2.5
15.01
15.3
0.0
4.48
9.96
15.3
25.7
$\Delta^{33}S$, ^{33}E (‰)
$\delta^{34}S$, $^{34}\varepsilon$ (‰)
18
16
14
2
0
−2
−4
−30
−25
−20
−15
−10
−5
0
5
10
15
20
25
30
24.25
25.7
15.01
15.3
10.65
9.96
4.48
15.01
15.3
9.96
25.7
15.3
15.1
4.48
9.96
SO_2 Pressure (italics, in mbar)
Calculated (This Report)
Residual SO_2 (Whitehill and Ono 2012)
Produced ^0S (Whitehill and Ono 2012)
Produced SO_3 (Whitehill and Ono 2012)

Figure 15.

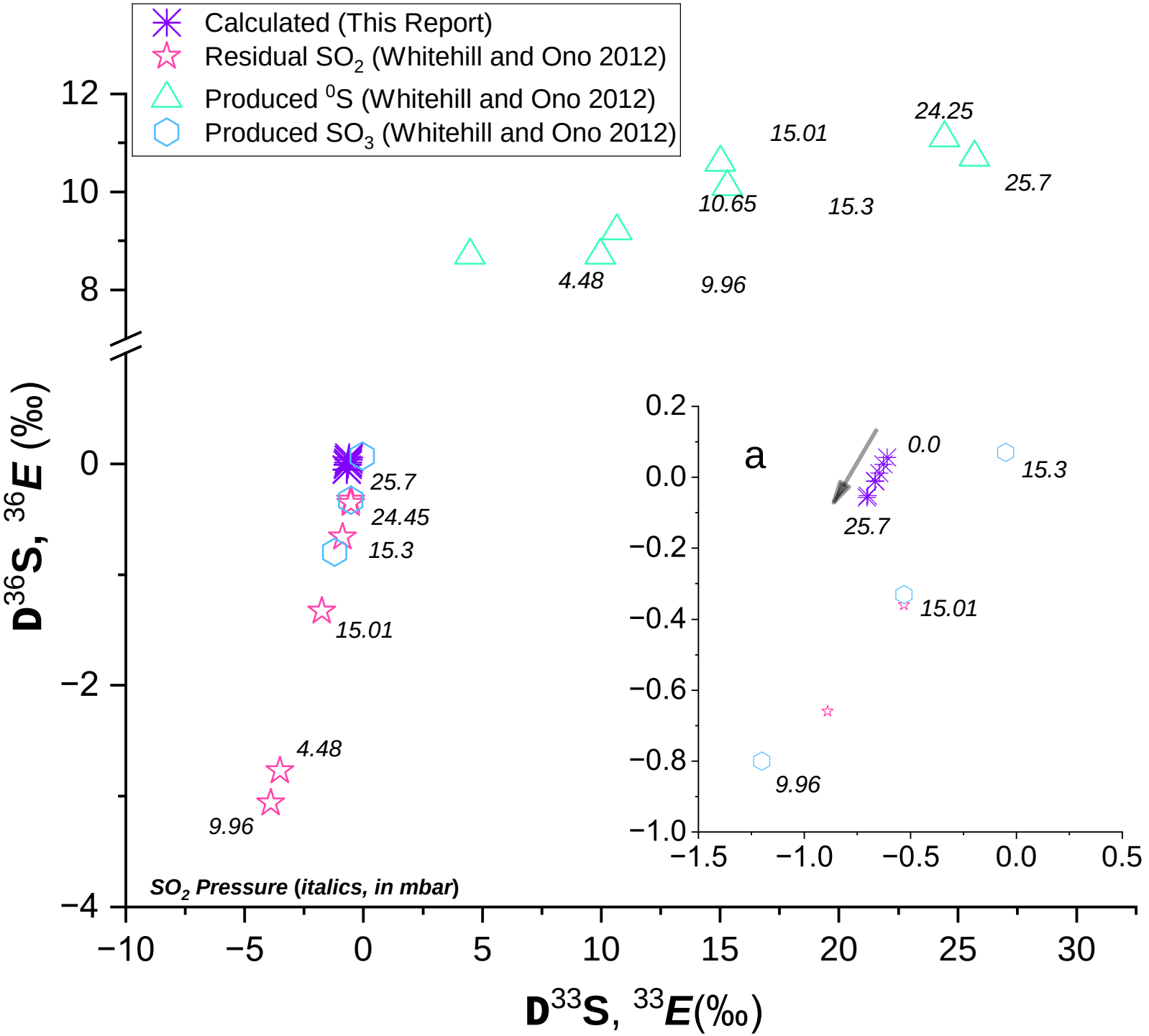
Calculated (This Report)
Residual SO2 (Whitehill and Ono 2012)
Produced 0S (Whitehill and Ono 2012)
Produced SO3 (Whitehill and Ono 2012)
24.25
15.01
25.7
10.65
15.3
4.48
9.96
25.7
24.45
15.3
15.01
4.48
9.96
a
0.0
15.3
25.7
15.01
9.96
SO2 Pressure (italics, in mbar)
D36S, 36E (‰)
D33S, 33E(‰)

Figure 16.

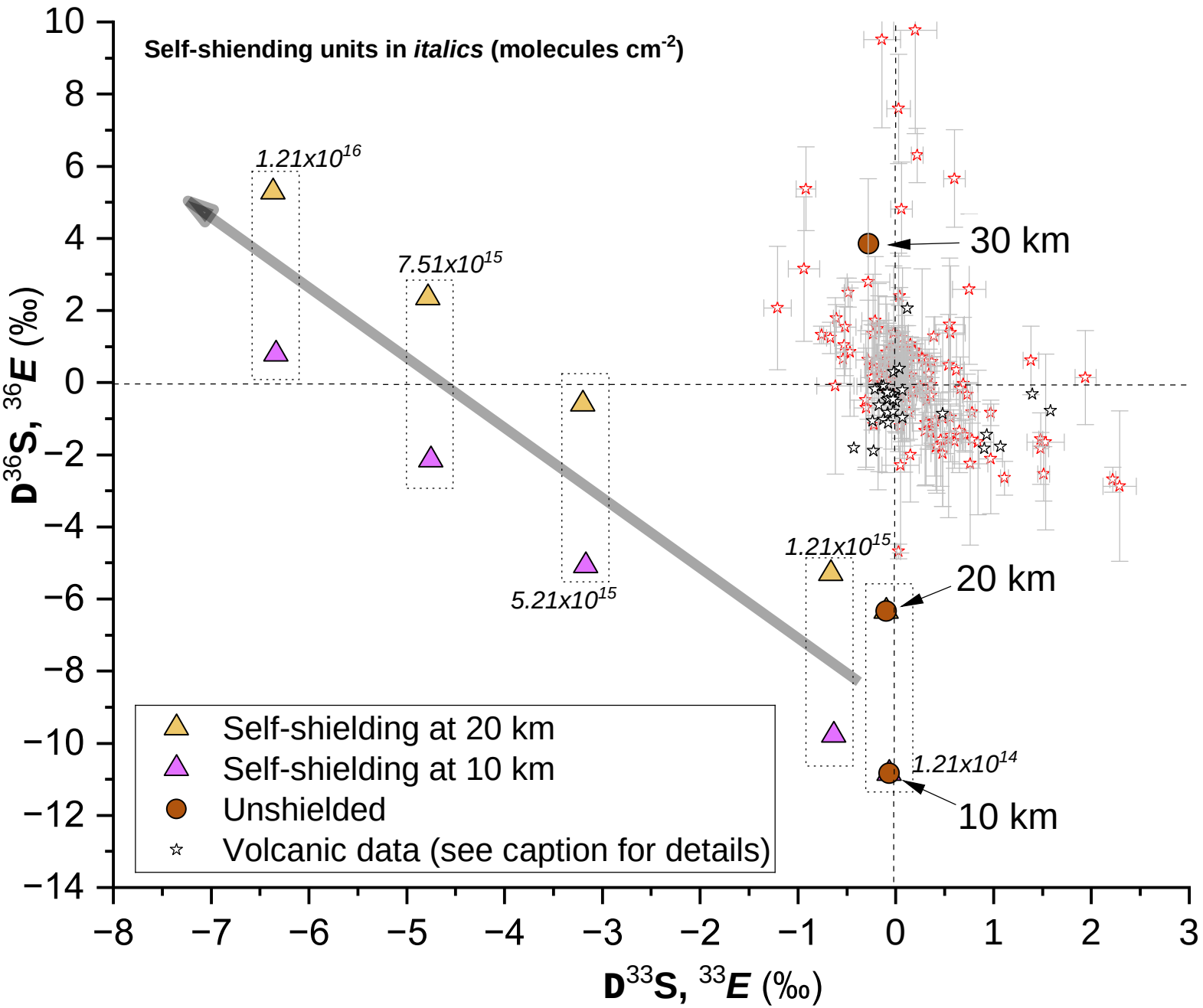
Self-shiending units in *italics* (molecules cm^{-2})
1.21x10^{16}
7.51x10^{15}
5.21x10^{15}
1.21x10^{15}
1.21x10^{14}
30 km
20 km
10 km
Self-shielding at 20 km
Self-shielding at 10 km
Unshielded
Volcanic data (see caption for details)
D^{36}S, ^{36}*E* (‰)
D^{33}S, ^{33}*E* (‰)
10
8
6
4
2
0
−2
−4
−6
−8
−10
−12
−14
−8
−7
−6
−5
−4
−3
−2
−1
0
1
2
3

Figure 17.

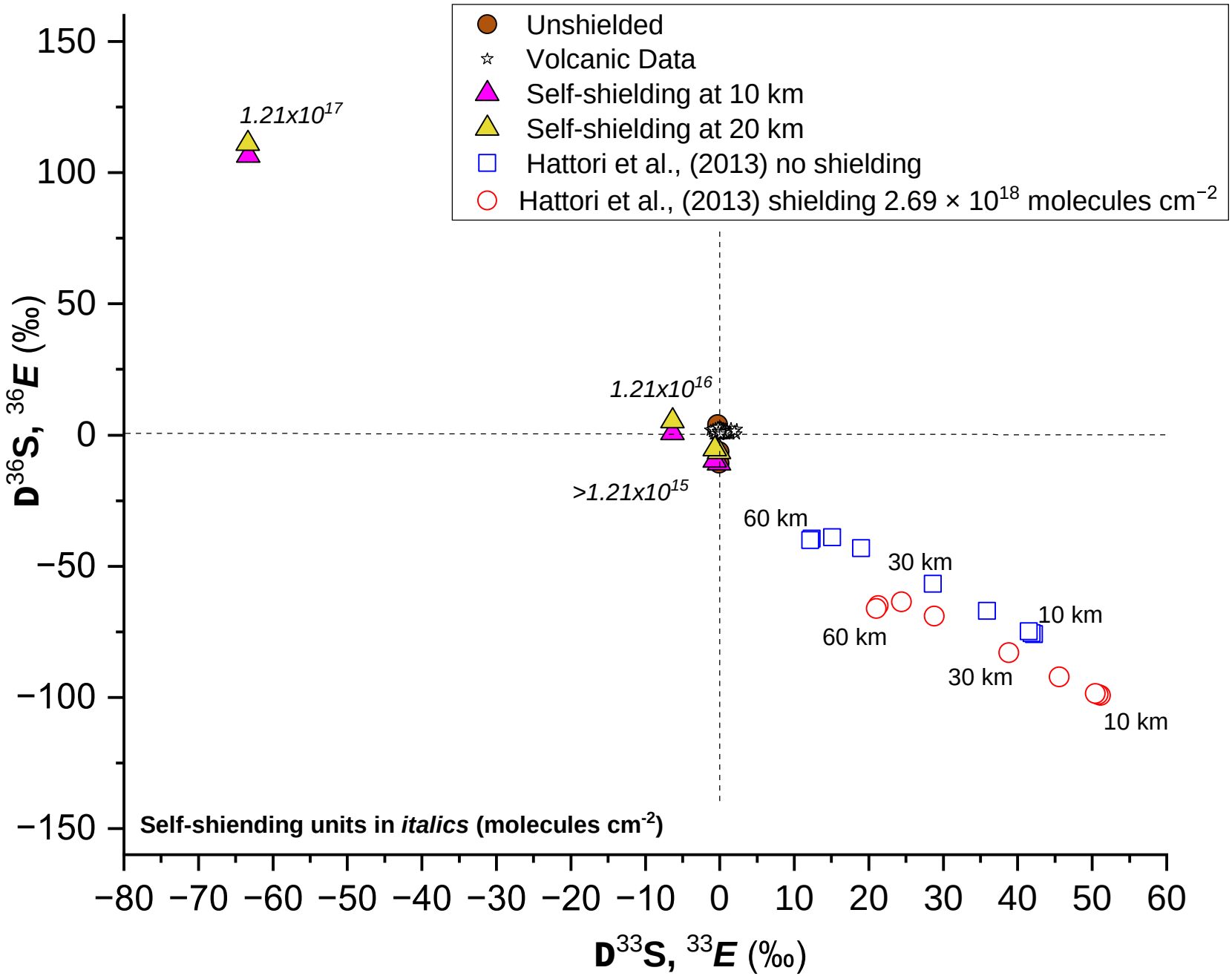
Unshielded
Volcanic Data
Self-shielding at 10 km
Self-shielding at 20 km
Hattori et al., (2013) no shielding
Hattori et al., (2013) shielding 2.69 × 10^18 molecules cm^−2
1.21x10^17
1.21x10^16
>1.21x10^15
60 km
30 km
10 km
60 km
30 km
10 km
Self-shiending units in italics (molecules cm-2)
D36S, 36E (‰)
D33S, 33E (‰)
150
100
50
0
−50
−100
−150
−80 −70 −60 −50 −40 −30 −20 −10 0 10 20 30 40 50 60